ORIGINAL ARTICLE

The influence of porosity on Ti-6Al-4V parts fabricated by laser powder bed fusion in the pursuit of process efficiency

Wen Hao Kan[1,2] · Mu Gao[1,2] · Xi Zhang[3] · Enquan Liang[3] · Ngai Sum Louis Chiu[1,2] · Chao Voon Samuel Lim[1,2] · Aijun Huang[1,2]

Abstract

In this study, the influence that porosities play on the mechanical properties of Ti-6Al-4V parts fabricated by laser powder bed fusion (LPBF) was investigated with the aim of improving process efficiency of the LPBF process by establishing the resulting trade-offs to component quality. It was found that build times can be substantially reduced by using higher layer thickness parameters without a significant detriment to mechanical properties. Where porosities formed, spherical pores tend to have a marginal effect on Young's modulus, yield strength, tensile strength, and uniform elongation as these properties can be approximated linearly using the rule of mixtures assuming null strength pores. However, such pores were found to be otherwise more detrimental to total elongation and toughness. Conversely, lack of fusion pores are extremely detrimental and should be avoided. Thus, it is proposed that when building a component, different process parameters can be used at different regions of the component to maximize process efficiency without compromising its overall function. For instance, for surfaces, a highly optimized parameter set with lower layer thickness can be used. At regions with minimal stress distribution during service, a large layer thickness parameter set where the resulting mechanical properties is sufficient can be used.

Keywords Additive manufacturing · Titanium alloys · Mechanical properties · Porosity · Process efficiency

Wen Hao Kan and Mu Gao contributed equally to this work.

Highlights
- Different LPBF parameters can adapted to localized requirements across a component.
- This approach can minimize build times without compromising component function.
- The amount and type of pores result in predictable trends to mechanical properties.
- Total elongation and toughness are severely affected by even small amounts of pores.
- In pursuing process efficient parameters, lack of fusion pores should be avoided.

✉ Wen Hao Kan
  wenhao.kan@monash.edu

✉ Aijun Huang
  aijun.huang@monash.edu

1 Monash Centre for Additive Manufacturing, Notting Hill, VIC 3168, Australia

2 Department of Materials Science and Engineering, Monash University, Clayton, VIC 3800, Australia

3 Commercial Aircraft Corporation of China Ltd, Shanghai 200050, People's Republic of China

1 Introduction

Additive manufacturing (AM) has gained significant interest in recent years as a cost-effective method of fabricating components made out of Ti-alloys because, as compared to conventional manufacturing methods, the AM approach results in significantly lower material wastage and is able to build near-net shaped components that require significantly less machining [1, 2]. Laser powder bed fusion (LPBF), which is also known as selective laser melting or direct metal laser sintering [3, 4], is an AM technique where a component is built layer by layer through the melting and fusing of metallic powder that has been dispensed across a platform with the use of a high-powered laser. Among Ti alloys, Ti-6Al-4V is perhaps the most investigated for LPBF due to its prevalence in the aerospace and biomedical industries [5, 6]. It should be noted, however, that in the as-built condition, an LPBF Ti-6AL-4V part has a brittle martensitic structure and for most applications, heat treatment is required to transform this phase into a combination of α and β phases so that a desirable combination of strength and ductility can be achieved [7].

It is well-known that one of the major limitations of LPBF is the inability to produce a component that is truly porosity-free. The extent by which porosities form is affected by both the processing parameters of the LPBF process as well as the way the inert gas flows across the building platform [5]. The two main types of porosities are lack of fusion pores and gas pores, the former is caused by insufficient melting and fusion of the metallic powders, and the latter is due to gases in the melt-pool that remain trapped as the melt rapidly solidifies [5]. Naturally, the presence of porosity is detrimental to mechanical properties, especially fatigue performance. As gas pores are often much smaller and spherical while lack of fusion pores are much larger and have irregular shapes, lack of fusion pores are much more detrimental to fatigue performance than gas pores [8]. Thus, a considerable amount of effort has been dedicated to minimizing the amount of porosity in structural LPBF Ti-6Al-4V components [9].

However, it is worth pointing out that for structural components that are not subjected to cyclic loading, these components may be able to fulfill their design requirements despite containing some amount of porosity. In such cases where a near-perfectly dense material is unnecessary, it may be much more economical to pursue process efficiency in the LPBF process (i.e., faster build times) [10]. In fact, process efficiency is a particularly important consideration for series production of components [11]. The trade-off between part density and process efficiency can be easily illustrated using the energy density equation:

$$E = \frac{P}{v * t * h} \tag{1}$$

where E is the energy density, P is the laser power, v is the scan speed, h is the hatch spacing, and t is the layer thickness) that is very commonly used to determine the process window required to produce a near fully-dense part [12, 13]. Based on this relation, laser power is the only parameter that has no influence in the building time. It is also worth noting that layer thickness has a comparatively greater influence on build time than scan speed and hatch spacing because it directly affects the amount of time that the LPBF system spends on powder recoating for a given build.

While it is easy to assume that based on the energy density relation faster build times can be achieved by simply increasing the laser power to compensate, all LPBF systems have a maximum laser capacity. Thus, in order to increase process efficiency, there has been an increasing focus on the development of high laser-power LPBF systems that are equipped with multiple lasers. However, it has been noted that the use of a high laser power can also lead to higher thermal gradients which result in higher residual stresses and an increase in cracking susceptibility

[14]. Regardless, the cooling rate or temperature gradient should be reduced during fabrication if possible and it has been established that increasing the scan speed and lowering the laser power would decrease the temperature gradient while increasing the layer thickness reduces residual stresses due to decreased cooling rates [6]. In this regard, the push for faster build times without excessively high residual stresses inevitably leads to a lower energy density that can result in the generation of pores. Therefore, for a given component, it is important to consider whether a near-perfect density is necessary for service and if not, process efficiency is certainly worth pursuing from an economic standpoint.

Additionally, when a structural component is used in service, the stresses that are distributed across the entire component are rarely uniform. Thus, regions of a given component where the stress loading is lower can also be fabricated using faster LPBF parameters since the presence of pores will be less of an issue while regions that have higher stress loading can be fabricated using LPBF parameters that are optimized for part density. In other words, the LPBF process parameters can be adapted to the requirements of specific locations in a component such that a faster building speed can be achieved without compromising the mechanical performance of the component. In fact, in more extreme cases where the stress distribution is minimal, the LPBF parameters can even be used to achieve very high levels of porosity for weight reduction purposes, a strategy demonstrated by Kim et al. [9] to fabricate porous Ti. Additionally, since a higher layer thickness results in poorer surface geometric accuracy, the adaptive method allows near-surface regions of a component to be built with a lower layer thickness, while the bulk of the component can be built with a higher layer thickness to pursue faster building times.

On the other hand, surface regions of a component can be fabricated using processing parameters dedicated to minimizing surface roughness, in which the angle of the surface and whether the surface is an up-skin or down-skin, may also need to be considered [15–17]. While the quality of the surface of the component is also dictated by contour scans, the contour scan is generally very thin (less than 0.5 mm) and appropriate bulk parameter set(s) can be used for the interior. The adaptive approach also means that the results of studies that have investigated the influence of LPBF parameters on a number of component properties, such as the one reported in [18], can be used more effectively by deriving and assigning the best parameter set based on the localized requirements of a given component as opposed to choosing a single parameter set for an entire component that is simply based on achieving the required properties that are most critical for it to function. In fact, it is possible to argue that this approach can

also be potentially used in fatigue-critical components. Studies have shown that for LPBF Ti-6Al-4V parts, as the fatigue life approaches the very high cycle regime, there is often a transition from surface pores being critical to bulk porosity being more critical [19, 20]. Thus, below the very high cycle fatigue regime, it may be possible for the bulk of a component to be fabricated using fast parameters without a significant detriment to fatigue life as long as the surface regions are highly optimized to contain near-zero porosity. In fact, this very argument has been made by Andreau et al. [21], though for LPBF 316L parts. Additionally, if hot-isostatic pressing is to be performed on the part anyway, then there is no reason why fast parameters are not used at the bulk regions, assuming that the pores can be closed [20].

Some have also proposed the use of lattice structures as a means to achieve faster build rates. Flores et al. [22] conducted a comprehensive study on the use of lattice structures for process efficiency, weight reduction, and raw material cost-saving. The authors noted that lattice structures require a high feature resolution to be built and that time savings are due to a reduction in overall scan area. This means that a low layer thickness is required for the former and the latter assumes that the same LPBF parameters are used between the lattice structure and a fully dense counterpart (i.e., optimized for material density). In other words, the improvement to build time is directly related to the volume fraction of the lattice structure. The authors showed that when lattice structures are built instead of a fully dense structure, a volume fraction reduction of 85% and 70%, resulted in a corresponding 59% and 49% reduction in LPBF manufacturing time, respectively [22]. Lattice structures are therefore, to be used in regions of a component that can inherently tolerate high amounts of porosity (which is the premise of using a lattice structure in the first place) such that only minimal load bearing capacities are required. However, these are also precisely the regions that can be built using high layer thicknesses and very fast scan speeds, a combination that can achieve a much greater reduction in build time without a significant compromise to the volume fraction of solid material. The latter is an important consideration because it means that the compromise to mechanical properties should be comparatively minimal. Thus, because lattice structures are an extremely inefficient method to reduce build times, they should only be used primarily as a means of achieving weight-reduction and cost-reduction (since less raw material is used), and any improvement to process efficiency should be viewed as a useful consequence rather than as the objective.

Naturally, in order for the process efficient or adaptive LPBF approach to work, the influence of porosity on mechanical properties must be understood so that the appropriate tolerances can be established. It should be noted that there have been several studies reported on the detrimental effects of porosity on the tensile behavior of LPBF Ti-6Al-4V parts. Liu et al. showed that samples containing predominately irregular-shaped pores would experience premature fracture resulting in poorer strength and ductility [23]. Keschel et al. reported that reducing porosity improves strength and ductility of LPBF Ti-6Al-4V parts only up to a certain point [24]. Montalbano et al. found that for similar amounts of porosity, LPBF Ti-6Al-4V samples with predominately lack of fusion pores tend to have lower yield strength, tensile strength, and Young's modulus as compared to samples containing keyhole pores, and ductility was substantially lowered in both cases as the porosity level increased [25]. In these cases, the issue with irregular-shaped lack of fusion pores has been attributed to increased stress-concentration points and the promotion of pore coalescence, both of which are in addition to the fact that pores reduce the actual volume of material available for load bearing. Similar observations have also been made by other authors for this material [26, 27]. Similar reasons have also been reported for the detrimental nature of lack of fusion pores on the impact toughness of LPBF Ti-6Al-4V parts [28, 29].

Thus, it is clear that the presence of pores, especially lack of fusion pores, are expected to be detrimental to tensile and toughness properties. In light of the available literature, the purpose of this study is to provide a more comprehensive understanding of how porosity can affect both the tensile and toughness properties of LPBF Ti-6Al-4V parts but with a focus on improving process efficiency without compromising component function, and whether there might be a way to easily predict these properties based on the amount of porosity present. Since lack of fusion pores tend to be oriented perpendicularly to the build direction, all mechanical test samples are built such that these pores are aligned parallel to the tensile axis and perpendicular to the impact direction (i.e., built horizontally along the building platform [28, 30]). This minimizes the influence that lack of fusion pores plays on mechanical properties, which also reflects the preferred tensile orientation at which a component should be built to minimize the detriment to mechanical properties when process efficiency is pursued.

2 Materials and methods

The Ti-6Al-4V powder used for this study was purchased from AP&C (GE Additive, Canada), and was specified to have a powder particle size of between 15 and 45 μm (D10: 22 μm, D50: 34 μm, D90: 45 μm) and a specified composition as shown in Table 1. For the LPBF process, the EOS M290 (EOS GmbH, Germany) was used. The build plate configuration, CAD file slicing, and processing parameter selection were all done using Magics 19.0 (Materialise, Belgium), RP-Tools 6.2.13 (EOS GmbH, Germany), and

Table 1 Nominal composition (wt%) of the powder used for the LPBF process as supplied by AP&C. Ti is balance

Al	V	Fe	O	C	N	H
6.09	3.94	0.20	0.107	0.019	0.009	0.002

EOSPRINT 1.9 (EOS GmbH, Germany). Prior to loading the powder into the system, the powder was first sieved using a 63 μm sieve. Due to spatial constraints, the metallographic specimens and the mechanical test samples were printed on two separate builds. Two different layer thicknesses were investigated — 30 μm and 60 μm. The processing parameters chosen for the 30 μm samples were designed to investigate a wider range of energy densities to investigate the influence of pores on mechanical properties, while the processing parameters for the 60 μm samples were chosen primarily for process efficiency without a significant compromise to part density. The processing parameters investigated are shown Tables 2 and 3 for the 30 μm and 60 μm layer samples, respectively. For simplicity, all parameter sets will be referred to with a number and alphabet which denotes their layer thickness and their relative build speed with respect to other samples of the same layer thickness (for instance, 30A and 30B are built using a 30 μm layer thickness, but 30A is a faster parameter set).

The metallographic samples were fabricated as 20 mm × 20 mm × 20 mm cubes. In order to show the viability of the adaptive LPBF process, the samples were printed with a "core–shell" structure where the core of each cube was built using the parameters outlined in Tables 2 and 3, while the shell of each cube was built using what is assumed to be a parameter set (Sample 30F in Table 2) that is optimized for part density at a layer thickness of 30 μm [7]. Thus, the samples built using the 60 μm parameters were done via layer skipping (i.e., laser scanning was done on alternate layers of 30 μm). The layer skipping method

Table 2 Process parameters of the 30 μm layer thickness samples arranged in decreasing order of build time

Sample ID	Scan speed (mm/s)	Laser power (w)	Hatch spacing (um)	Volumetric energy density (J/mm³)
30A	600	300	100	167
30B	600	250	140	99
30C	600	300	140	119
30D	700	292	140	99
30E	1000	200	140	48
30F	1200	280	140	56
30G	1500	300	140	48
30H	1600	160	140	24
30I	2300	200	140	21

Table 3 Process parameters of the 60 μm layer thickness samples arranged in decreasing order of build time

Sample ID	Scan speed (mm/s)	Laser power (w)	Hatch spacing (μm)	Volumetric energy density (J/mm³)
60A	600	300	80	104
60B	600	240	140	48
60C	600	300	140	60
60D	1200	280	80	49
60E	1200	200	80	35
60F	1200	280	140	28
60G	1400	300	140	26
60H	1400	240	140	20

was also used for the 60 μm samples on the build with the mechanical test samples so that these samples could be printed together with the 30 μm samples on the same build plate while also ensuring that the mechanical test samples were also built under similar conditions to that of the metallographic samples. After building, all samples were subjected to a stress-relief heat treatment of 800 °C for 6 h that also transforms the martensitic phase into a distribution of α and β phases that would result in a good balance between strength and ductility based on a study by Cao et al. [7]. The furnace took approximately 6 h to heat up to temperature, and the samples were furnace cooled.

The metallographic cubes were then sliced and sectioned. These samples were then mounted in conductive resin, ground, and polished. The final polishing step involved the use of OP-S colloidal silica solution (an active oxide polishing suspension supplied by Struers, Denmark). Microstructural information was obtained via scanning electron microscopy (SEM) using the 7001F (JEOL, Japan). Optical microscopy (OM, PMG 3, Olympus, Japan) was used to determine the amount and type of porosity in each sample. The amount of porosity was determined using grey-scale thresholding and segmentation on ImageJ across a minimum of five images (covering an area of at least 22 mm^2). It was found that there was minimal difference in porosity measurements across either orientation, and thus, the area fraction can be assumed to reflect the porosity level of the material. The porosity levels reported will be based on the "core" of the core–shell cubes as they reflected the porosity levels caused by the processing parameter sets of interest. Additionally, ImageJ was also used to analyze the average pore circularity for a given sample, which is defined as

$$\text{Circularity Factor} = 4\pi\left(\frac{A}{p^2}\right) \tag{2}$$

where A is the area of the pore and p is its perimeter. A circularity factor of 1 represents a perfect circle, and values

less than 1 represent an increasingly elongated shape. The analysis was conducted along the *YZ* plane as this plane constituted the cross-sectional plane of the tensile axis and the fracture plane of the Charpy samples, a method similar to that proposed by Snell et al. which is useful for rapid porosity analysis of AM metals [31]. For ease of reference, whenever a sample is referred to in the text, where relevant, it will also be accompanied by its average circularity factor (CF) and its porosity level (P).

The tensile samples were tested as sub-size flat dog-bone samples with a gauge width of 6 mm, gauge length of 25 mm, and a total length of 100 mm. These samples were built horizontally in the dog-bone shape and aligned parallel to the recoater direction. They were built as blocks 35 mm tall and were sliced into samples with a thickness of 3 mm. The tensile tests were based on ASTM E8 [32] using a ZwickRoell 100 kN universal testing machine and a Zwick-Roell BT2 extensometer (ZwickRoell, Austria). The strain rate was set at 0.45 mm/min before yielding and 9 mm/min after yielding. Charpy impact tests were conducted using the ZBC2302-CE (MTS, China), and the Charpy specimens were also built horizontally (aligned along the *X*-direction of the platform). Each Charpy specimen was built directly into shape (i.e., 55 mm long, 10 mm thick, and with the V-notch built, not machined) but as a 35-mm-tall block which was then sliced to form three Charpy specimens. The schematic of the mechanical test sample build is shown in Fig. 1a, and the tensile and Charpy blocks are shown in Fig. 1b, c. It should be noted that while sample location on a build plate (not just in the *X* and *Y* directions, but also in the *Z* direction) can influence the amount of porosity formed and the resulting mechanical properties of LPBF Ti-6Al-4V samples, it has been shown that this plays a much smaller effect as compared to the processing parameters used [33, 34]. Thus, as this study involves the comparison of samples built using different processing parameters, it will be assumed that effects of sample location do not play a significant role in porosity generation and mechanical properties.

The process efficiency of each parameter set investigated was based on the build time estimation function on the EOSPRINT software that was used to prepare the CAD files required for the LPBF process. A rectangular block with dimensions of 79 mm × 79 mm × 150 mm was used for this estimation to approximate a component with a build height of 150 mm that occupies ~ 10% of the volume of the build chamber at that height. For the 60 μm layer thickness estimation, it was assumed that there would be no difference in material quality if the samples were built using 60 μm layer thickness or by alternate layer skipping at 30 μm layer thickness. The main difference between the two is that the former method would be used if process efficiency is to be maximized, while the latter would be used if the adaptive LPBF method is pursued. Naturally, layer skipping results in
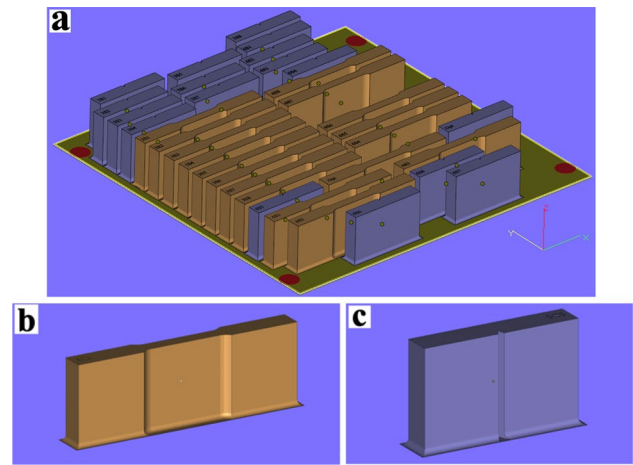

Fig. 1 The samples of the mechanical testing build are organized as shown in (**a**). The tensile (**b**) and Charpy samples (**c**) are built into shape along the *XY* direction but as blocks with a height of 35 mm to be sliced into several samples after building. Note that there are also samples that were printed on the build that are not part of this study. These samples are not shown in (**a**)

a slower build time since the advantage of reducing the time spent on powder recoats is eliminated. To highlight this, the build time will be estimated for the 60 μm layer thickness samples using both approaches.

3 Results and discussion

Figure 2 shows the metallographic analysis of the sample fabricated with parameter set 60A. Figure 2a, b are low magnification backscatter electron (BSE) images across the interface of the core–shell region of the cube which show that there is a clear delineation between a region with higher porosity and a region with minimal porosity without an abrupt change in the microstructure across the interface. It is also worth noting that the porous region was built with a layer thickness of 60 μm as opposed to the optimized region at 30 μm. Figures 2c, d are higher magnification images that show that the microstructures of the porous and optimized regions are essentially identical.

Figure 3a, b show the build time estimation of the various 30- and 60 μm parameter sets, respectively. With regard to the latter, the effect of layer skipping is also shown. As was mentioned previously, the build time estimation is based on the building of a 150-mm-tall component that occupies 10% of the entire build volume. For build height of 150 mm, a 30 μm build and a 60 μm build with layer skipping would both require 5000 recoats. However, a 60 μm build without layer skipping only requires 2500 recoats. A direct comparison between the 60 μm parameter sets with and without layer skipping (yellow and red in Fig. 3b, respectively), which is
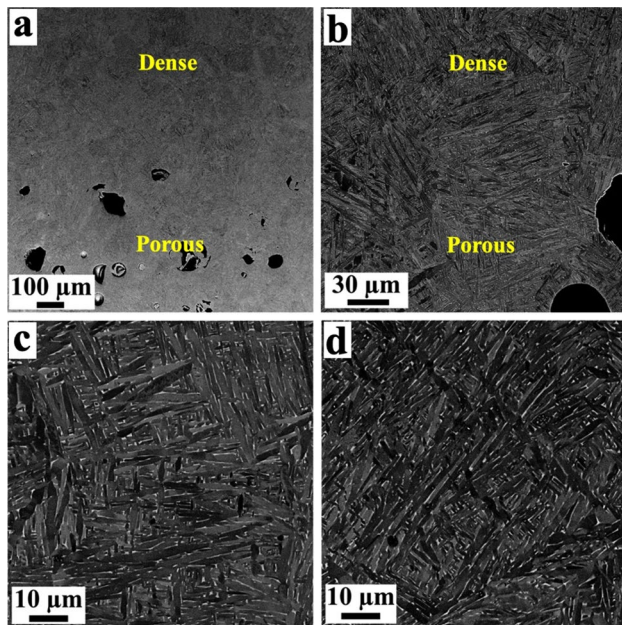
Fig. 2 Metallography analysis of the cube along the *XY* plane where the "core" was fabricated using parameter set 60B: **a** low magnification BSE SEM image showing the interface region between the "porous" core and the optimized "dense" shell, **b** a BSE image that shows a lack of a microstructural interface between the two regions, **c** a high magnification BSE image that show the microstructure of the porous core, and **d** a high magnification BSE image that shows the microstructure of the optimized shell

a difference of 2500 recoats, amounted to a time difference of 7 h. A comparison between 30 and 60F, which are identical except in terms of layer thickness, shows that doubling the layer thickness essentially halves the building time (73 vs 36 h) assuming that there is no layer skipping in the latter. Comparing 30B and C confirms that laser power has no influence on build time, and comparing both of them to 30F shows that doubling the scan speed only reduces the build speed by 41% as opposed to 50% simply because the time spent recoating cannot be saved through altering the scan speed. Figure 4 shows the OM images of the porous regions of all samples that were printed using parameter sets that resulted in porosity levels that are greater than 0.5%. Parameter sets 30H and 30I resulted in excessively high amounts of pores that could potentially be somewhat interconnected in three-dimensions.

The various mechanical properties that correspond to each sample are shown in Fig. 5, while Fig. 6 shows the typical stress–strain curves for some of the parameter sets. For most samples that achieve the expected tensile strength for the material (~1000 MPa), the figure also highlights how at higher porosity levels, there tends to be premature fracture without substantial elongation after the maximum stress has been reached (i.e., limited ability to neck without breaking).

To better understand how porosity levels affect the mechanical properties of the samples, the mechanical test results shown in Fig. 5 were plotted against the porosity level of their respective samples. The resulting graphs are shown in Fig. 7. One method of estimating the contribution of porosity to mechanical properties is to use the rule of mixtures, a method that is commonly used to estimate the mechanical properties of composites except that for a porous material, the pores can be assumed to be the second phase with its mechanical properties assumed to be zero [35]. Given that the porosity (*p*) is small, the rule of mixtures can be simplified as

$$\frac{M_c}{M_s} = (1-p)^{\frac{1}{J}} \tag{3}$$

where M_c is the mechanical property of the material that contains the pores, M_s is the mechanical property of its fully dense counterpart (i.e., the same material without pores), *p* is the porosity fraction, and *J* is a material parameter which is usually equal to one or less [35]. It should be noted that this expression assumes that the increase in porosity from the ideal fully dense alloy does not alter its intrinsic microstructure. In reality, changes in porosity levels brought about by different processing parameters can also alter the microstructure, and when the porosity in the alloy approaches zero (but will most likely not be zero in actual LPBF alloys), mechanical properties will be increasingly dictated by microstructure variations [36]. When *J* is equal to one, the mechanical properties of the material would decrease linearly to zero as the amount of porosity is increased up to 100%. On the other hand, *J* equals zero represents the extreme situation where the mere presence of porosity causes the material to essentially have zero mechanical properties. For a given amount of porosity, the shape of the pores plays a crucial role in determining the J factor (for instance, irregular shaped pores will have a lower *J* value than round shaped pores) [35]. The rule of mixtures, assuming that *J* = 1, are illustrated by the dash lines in Fig. 7. As can be observed in Fig. 7a–c, the Young's modulus, yield strength, and tensile strength for most of the investigated samples generally follow the rule of mixtures. On the other hand, the uniform elongation results (at least partially), and especially the elongation at fracture and toughness results, do not actually follow the rule of mixtures when *J* = 1.

Pores formed due to lack of fusion during the LPBF process are generally irregular in shape, and can be distinguished from gas/keyhole pores through differences in sphericity and size [10, 37, 38]. Since it has been established that irregular-shaped pores result in a lower J value than rounded pores, it can be assumed that lack of fusion pores would be more detrimental to mechanical properties as compared to gas or keyhole pores which tend to be more spherical

Fig. 3 Build time estimates of **a** the 30 μm layer thickness parameter sets and **b** 60 μm layer thickness parameter sets based on building a 79-mm×79-mm×150-mm rectangular block, and **c** and **d** are the resulting porosity levels that correspond to those parameter sets, and **e** and **f** are the average sphericity values of the pores that correspond to those parameter sets
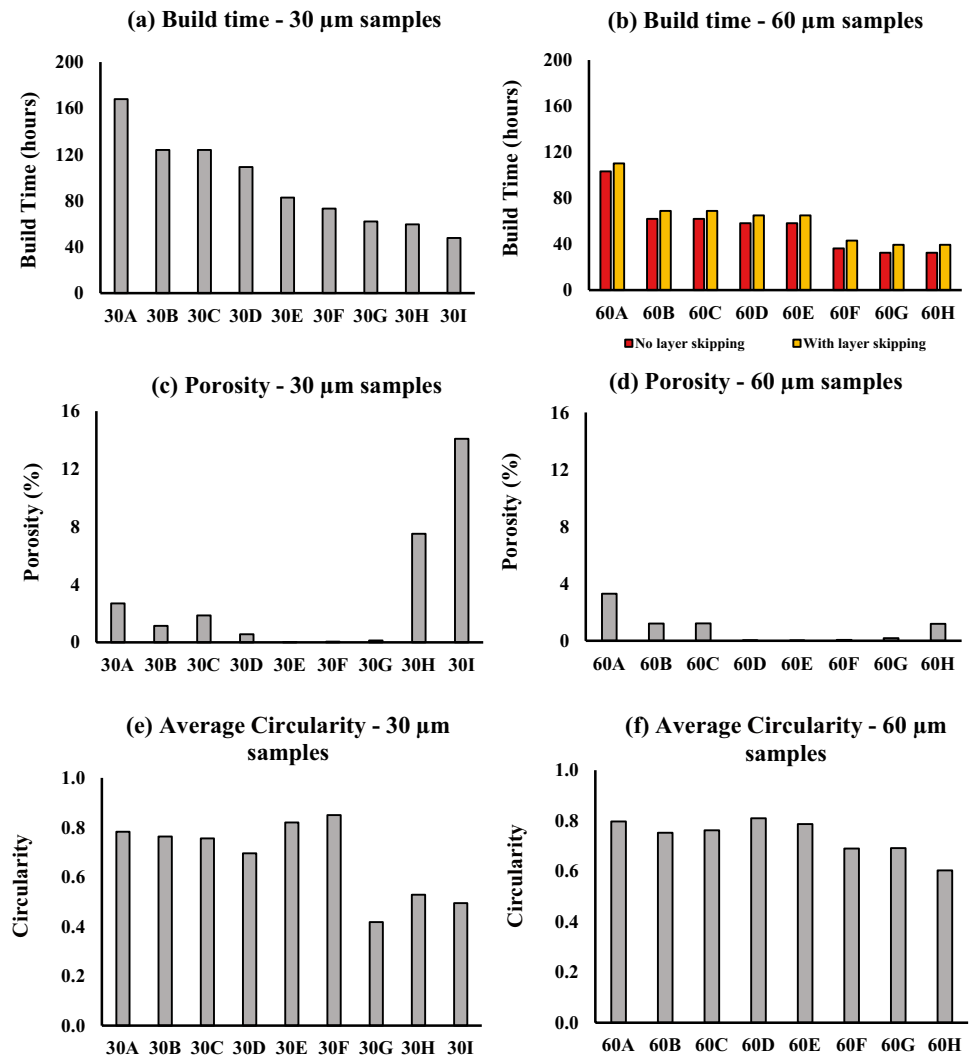
in shape. Regarding the porosity analysis conducted in this study, it is important to note that the purpose of this study is not to develop a 2D approach to systematically analyze/categorize the pore population in a given sample, but rather, to identify a simple way to predict mechanical properties in relation to the amount of porosity present, for instance, using the rule of mixtures where $J = 1$ assuming pores are mostly spherical. Since samples that contain more lack of fusion pores will have a lower average pore sphericity, this should also be reflected in a lower average circularity from 2D imaging analysis.

In trying to develop a rapid way to characterize pores, Snell et al. attempted several analysis methods to distinguish between lack of fusion, gas, and keyhole pores in a given material captured using 2D and 3D methods (i.e., optical microscopy and μ X-ray computed tomography) by relating circularity/sphericity factors to pore size or aspect ratio [31]. It should be mentioned that their 2D analysis methods were developed to categorize specific pore types in a given alloy

based on calculated porosity geometric (i.e., pore size and circularity) limits specific to the material. In this regard, their 2D approach is much less useful for the purposes of this study. However, in their 3D analysis, they found that a pore with a sphericity of 0.6 or less is almost always a lack of fusion pore while a pore with a sphericity of 0.9 or more is almost always a gas or keyhole pore, with the intermediate sphericities being mostly ambiguous. Based on this finding, if the average 2D circularity of all pores in a sample based on 2D optical microscope image analyses is less than 0.6, we can simply assume that this sample contains predominately lack of fusion pores.

However, when a circularity threshold of 0.60 was used, it was found that Sample 60G (CF: 0.69, P: 0.18%) has a lower Young's modulus, yield strength, tensile strength, and uniform elongation than what its porosity level would suggest. More importantly, its elongation at fracture (9.2%) and impact toughness (23 J) are far lower than expected for its porosity level. Thus, it appears that it would be more
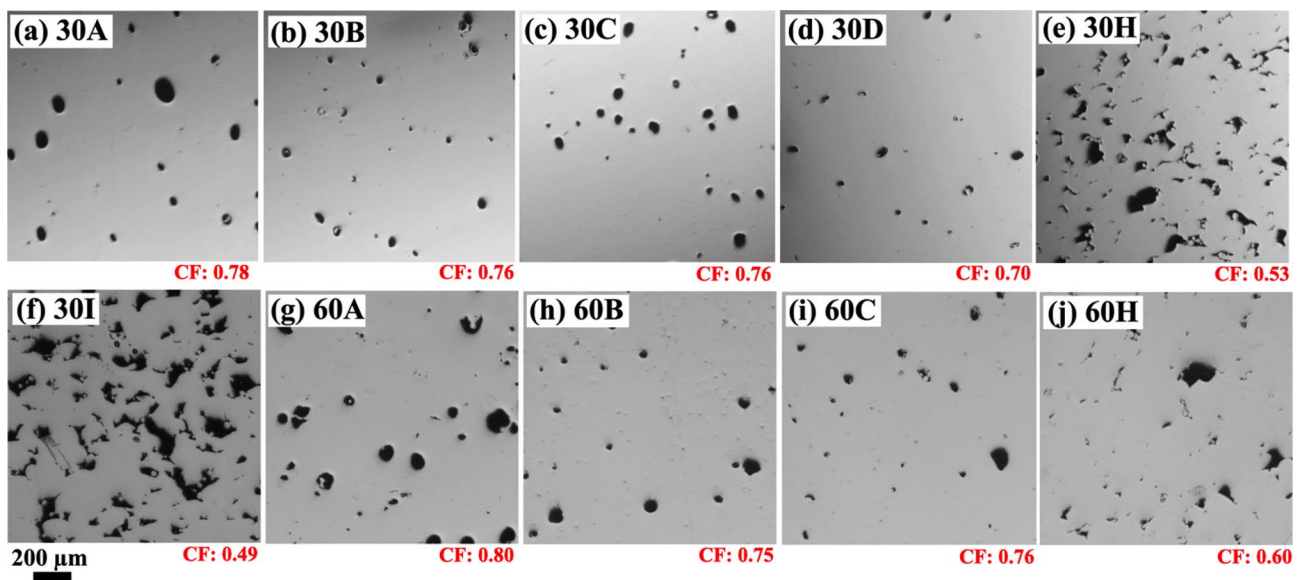
Fig. 4 OM images of parameter sets that resulted in porosity levels greater than 0.5%: (**a**) 30A, (**b**) 30B, (**c**) 30C, (**d**) 30D, (**e**) 30H, (**f**) 30I, (**g**) 60A, (**h**) 60B, (**i**) 60C and (**j**) 60H. The corresponding CF of each sample is shown in red at the bottom right corner of its image

meaningful to use a CF of 0.70 for the purposes of predicting mechanical properties. Interestingly, expanding the CF to 0.70 would also include Sample 60F (CF: 0.69, P: 0.06%) into this category, a sample that has similar Young's modulus, yield strength, tensile strength, and uniform elongation compared to other samples of its porosity level but much lower elongation at fracture (~11%). As for toughness, this sample performed identically (~30 J) to the lowest performing sample of comparable porosity that contained predominately spherical pores (Sample 60E, CF: 0.79, P: 0.02%).

To provide more information on the porosities of Samples 60G (CF: 0.69, P: 0.18%) and 60F (CF: 0.69, P: 0.06%), Fig. 8 shows the frequency distribution of pore circularity for these two samples. As can be observed, the pore circularity for 60G is generally uniformly distributed across the circularity range between 0.40 and 0.80. As most pores have a circularity below 0.70, this sample is likely to contain many lack of fusion pores with range of irregular morphologies. On the other hand, the pores in Sample 60F appear to be loosely separated into two groups, the first having a rather irregular morphology (circularity of 0.5~0.6) and the second being rather spherical (circularity of 0.8~0.9). This indicates that Sample 60F contains many spherical gas pores in addition to having a substantial population of lack of fusion pores. Thus, even though the porosity CF is similar for both samples, the nature of their porosities is different. Furthermore, considering the detrimental nature of irregular-shaped pores and the frequency of such pores in both these samples, using a CF threshold of 0.70 to predict the influence of porosity on mechanical properties appears to be more reasonable.

Therefore, Fig. 9 shows the graphs of all the mechanical properties but with the red data points representing the samples that have an average pore CF less than 0.70 and thus, are assumed to contain lack of fusion pores, and all other samples that contain mainly spherical pores in black. As can be observed, in most cases, samples that contain lack of fusion pores have significantly poorer mechanical properties than samples that have predominately spherical pores, even at the similar porosity levels. This also confirms that the type of porosity present may have a greater impact on mechanical properties than the amount of porosity present, especially to elongation at fracture and toughness. For instance, samples with low porosity levels that contain lack of fusion pores may still have modest Young's modulus, yield strength, tensile strength, and uniform elongation as compared to samples with similar fraction of spherical pores, but the former will have significantly lower elongation at fracture and toughness than the latter. In this regard, the results here are similar to those by Montalbano et al. where the authors showed that the yield strength, tensile strength, and Young's modulus of samples containing keyhole pores are generally linearly related to the porosity level, and samples containing lack of fusion pores performed much worse than these samples for a given porosity level [25]. However, their elongation results differed from this study in that both keyhole and lack of fusion pores were found to be almost equally detrimental. It is important to note that their samples were also built along the same orientation (parallel to the re-coater) and the investigated amount of porosity went up to 6% for keyhole samples and 8% for lack of fusion samples (though measured using X-ray computed tomography).
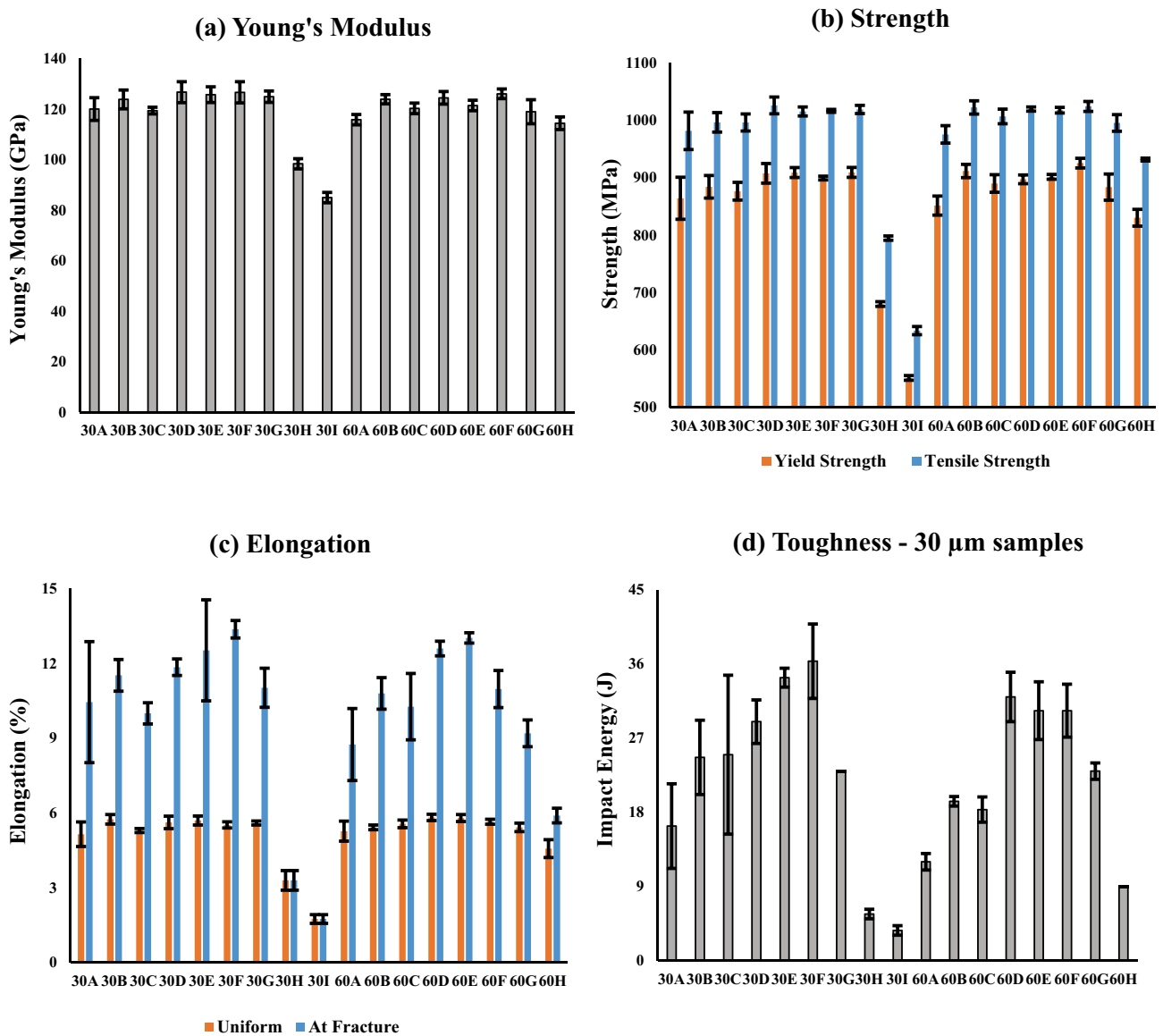
Fig. 5 Mechanical test results of all the samples showing **a** the Young's modulus, **b** the yield and tensile strengths, **c** the uniform elongation and elongation at fracture, and **d** impact toughness. 30F is the optimized parameter set. Error bars show the standard deviations

Generally speaking, the presence of porosity tends to reduce the tensile strength of a metal in proportion to the area occupied by pores across the cross-sectional plane that has the highest area occupied by pores but the mere presence of small amounts of porosity can substantially reduce ductility [39]. For example, Voisin et al. has shown that for LPBF Ti-6Al-4V samples containing less than 1% porosity, yield strength and uniform elongation are affected by intrinsic microstructure but the strain to failure is affected by pores [40]. If we consider the samples with spherical pores in Fig. 9, it can be observed that most of the mechanical properties have a linear trend in relation to porosity, but in reference to Fig. 7, it can be seen that only the yield strength and tensile strength perfectly follow the rule of mixtures

($J = 1$). While uniform elongation appears have a linear trend that is just marginally below the rule of mixtures ($J = 1$), the mere presence of porosity causes the elongation at fracture to drop significantly below what the rule of mixtures predicts. Thus, it can be said that our results are consistent with the findings of Voisin et al. in that at low levels of porosity (e.g., 1% or less), the effect of porosity should be negligible to yield strength and uniform elongation since there should not be more than 1% variation to these mechanical properties based on the rule of mixtures. That said, the larger scatter in our results for yield strength at near 0% porosity seem to suggest that microstructural effects play a bigger role to yield strength than for tensile strength and uniform elongation. Nonetheless, our study has shown that yield strength

Fig. 6 Stress–strain curves of the various parameter sets
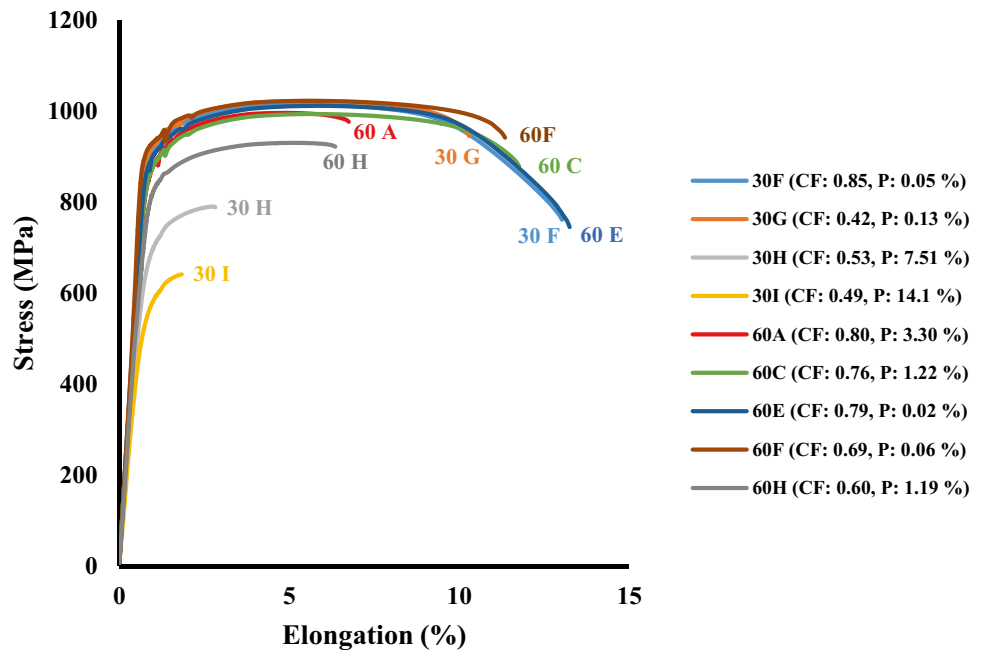
and tensile strength do continue to reduce proportionally to the amount of porosity present at higher levels of porosity as long as the pores are spherical, but this is marginally less so for uniform elongation.

Since the lack of fusion pores result in a substantial reduction in mechanical properties as opposed to spherical pores, it suggests that the irregularity in pore shape plays a greater role than the loss in area across the fracture plane. Since pore shape irregularity results in an increase in stress concentration due to increased local curvatures, this accelerates the initiation and propagation of cracks, and the growth and coalescence of pores [39, 41–43]. This is reflected by the comparison of the stress–strain curves for 60C (CF: 0.76, P: 1.22%) and 60H (CF: 0.60, P: 1.19%) in Fig. 6, where both materials had similar levels of porosity but the pores in 60H have a much lower average defect circularity (which can also be observed by comparing their respective OM images in Fig. 4i, j, respectively). On average, 60H yielded slightly earlier in the test (~830 MPa vs ~890 MPa) but fractured very shortly after reaching its tensile strength (~5.9% vs ~10.3% and ~930 MPa vs ~1000 MPa, respectively). As can be observed, the reduction in yield and tensile strengths may be marginal (~7% reduction) but the acceleration of fracture resulted in a substantial reduction in total elongation due to the inability to neck as a result of porosity coalescence and crack propagation (~43%).

An interesting comparison can also be made between Samples 60A (CF: 0.80, P: 3.30%) and 60H (CF: 0.60, P: 1.19%) as both have very similar stress–strain behavior (Fig. 6) but the former still has better mechanical properties on average (yield strength: ~850 MPa and ~830 MPa, tensile strength: ~980 MPa and ~930 MPa, and elongation

at fracture: ~8.8% and ~5.9%, respectively) despite having almost twice as much porosity. As can be observed with Fig. 4g, j, Sample 60A contains more pores (and hence higher porosity) on average but Sample 60H displays significantly fewer large-sized irregular pores. The fracture surfaces after tensile testing, shown in Fig. 10, explains the differences. Due to the pores in 60H being irregular, the fracture path easily propagates from one pore to another in 3D, often though the weakest orientation axis along a given pore. This leads to a fracture profile that is more convoluted in 3D (compare Fig. 10a, b). When analyzed at a higher magnification (Fig. 10c, d), the fracture surfaces of both samples are filled with traversed pores, but the fracture path in 60A travels through multiple spherical pores to cover a distance of several hundred microns but a fracture path of similar distance in 60H can be covered by simply traversing a single irregular-shaped pore along its most unfavorable orientation axis in 3D. Thus, despite 60H having a lower nominal porosity level, localized yielding within the material surrounding the pores would occur at lower load levels which leads to a slightly lower apparent yield and tensile strength while the poorer elongation at fracture is due to the facilitation of pore coalescence brought about by the large irregular-shaped pores.

Regarding toughness, it is known that the presence of porosity and a reduction in ductility (due to microstructural or compositional differences) can significantly reduce toughness [28, 30, 44, 45]. In this study, we found that a relatively small reduction in elongation at fracture due to the presence of porosity actually caused a substantial reduction in toughness, even for samples that contain mainly spherical pores. For instance, when comparing 60A (CF: 0.80, P: 3.30%)
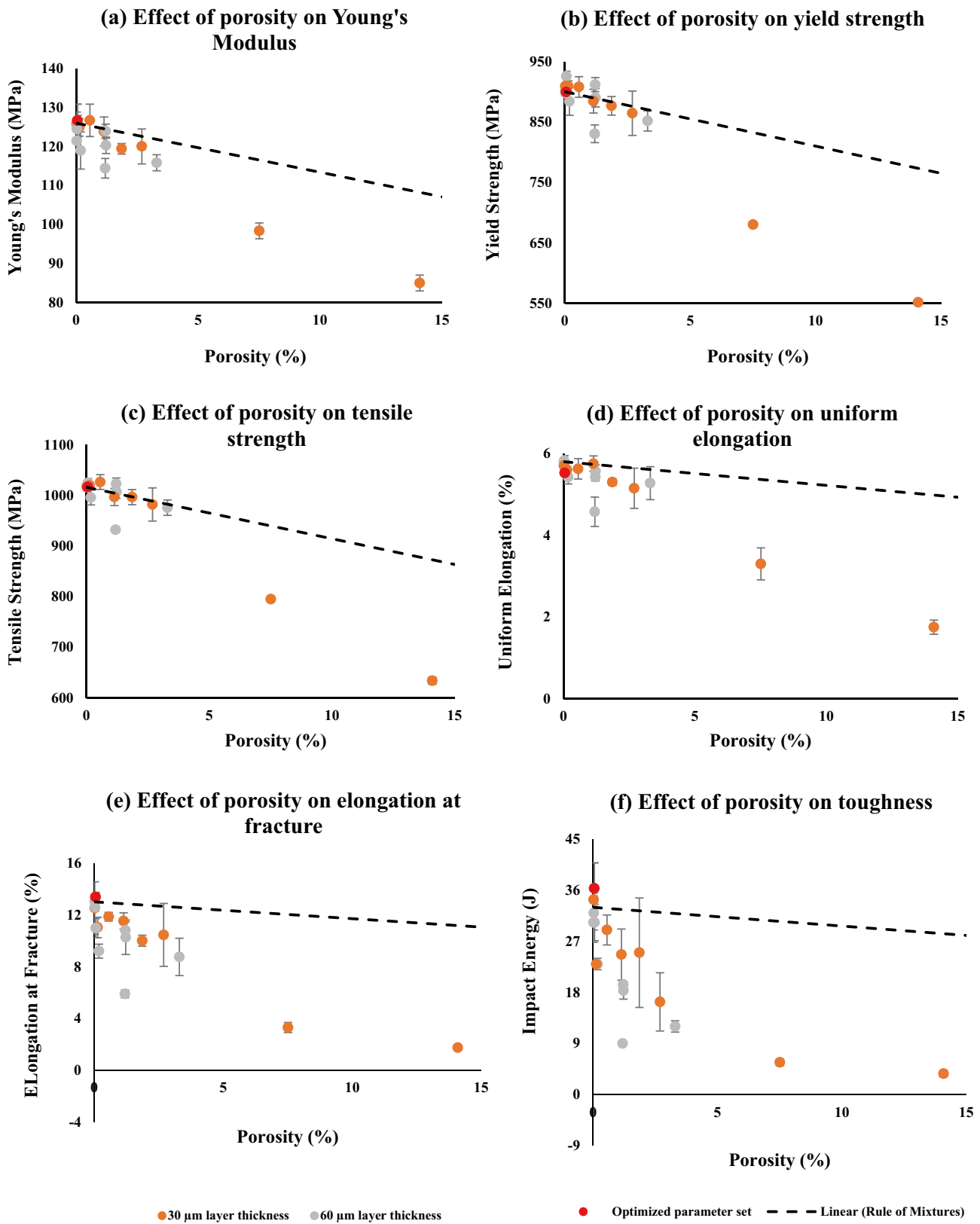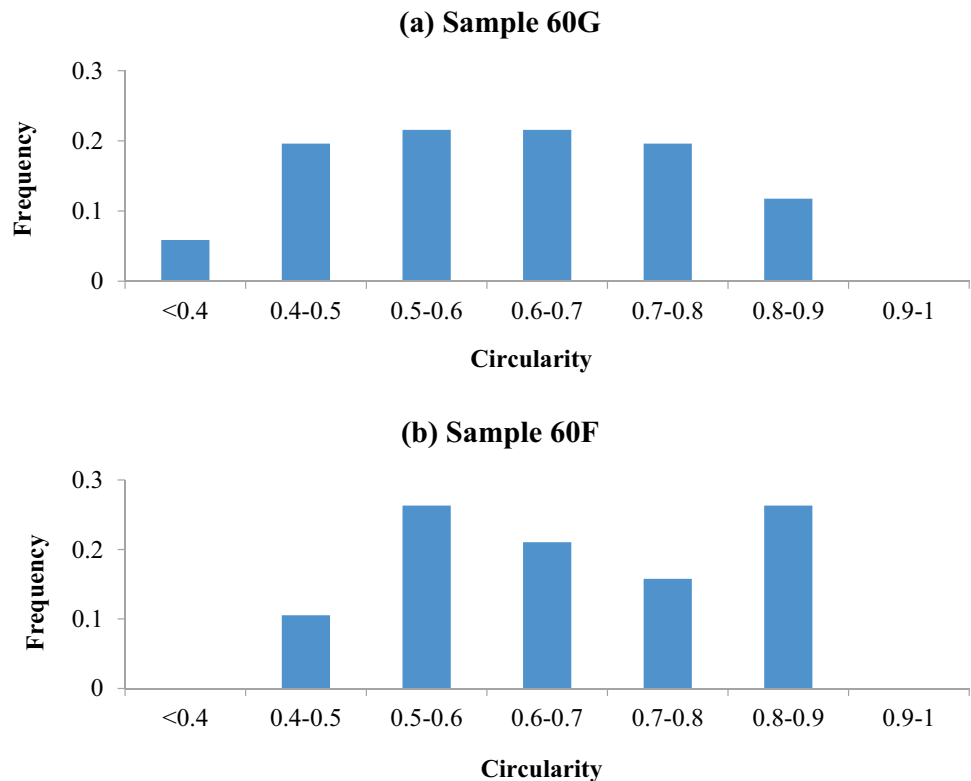
Fig. 7 Effect of porosity on mechanical properties —**a** Young's modulus, **b** yield strength, **c** tensile strength, **d** uniform elongation, **e** elongation at fracture, and **f** toughness. The dashed line represents the Rule of Mixtures assuming that $J = 1$

Fig. 8 Histograms showing the frequency distribution of pore circularity in samples **a** 60G and **b** 60F

(a) Sample 60G

(b) Sample 60F

to the optimized parameter set 30F (CF: 0.85, P: 0.05%), a reduction in ~ 35% ductility (from an average of 13.38% to 8.75%) resulted in a 67% reduction in toughness (from an average impact energy of ~ 36 J to ~ 12 J). Another useful comparison is between 30B (CF: 0.76, P: 1.14%) and 60C (CF: 0.76, P: 1.22%), with their mechanical properties summarized in Table 4. Both these samples have similar sized and shaped pores (refer to Fig. 4b, i) but 30B has a slightly lower porosity level than 60C which resulted in a marginally higher elongation at fracture but a substantial reduction in toughness despite all other mechanical properties being essentially equal. Since a strength/ductility trade-off was not observed in this case, microstructural differences are unlikely to be a contributing factor. Figure 11 shows the SEM images of their respective Charpy fracture surfaces which confirms that the types of pores in both samples are very similar, thus indicating that it is the amount of porosity, not porosity type, that caused the difference in the elongation at fracture and toughness results. This could indicate that toughness is particularly sensitive to the amount of pores present.

While the reduction in total elongation is mostly responsible for the reduction in toughness, the reduction in strength and Young's modulus due to the presence of porosity cannot be discounted entirely since these are properties that also affect how stresses are distributed during impact [46]. Interestingly, for samples that contain predominately lack of

fusion pores, when porosity levels exceed 1%, elongation at fracture and toughness start to display near-linear reductions (after a substantial reduction between 0 to 1%) as a function of porosity levels. This is despite the fact that the nature of the lack of fusion pores can be substantially different between samples that contain low amounts of lack of fusion pores and samples that contain high amounts of lack of fusion pores.

Another explanation why the Young's modulus, yield strength, tensile strength, and (to a lesser degree) uniform elongation of samples containing spherical pores tend to follow the rule of mixtures but elongation at fracture and toughness do not, could be due to the fact that the latter two are properties that are directly affected by the coalescence of voids/pores [24, 25, 29]. As was shown in the study by Voisin et al. [40], once pore coalescence and growth occur, the real volume fraction of pores rapidly increases up to the point of fracture. However, the direction in which the pores grow and coalesce is dependent on the tensile axis and is therefore, not isotropic. Therefore, because the $J = 1$ assumption is based on pores being spherical and that the amount of porosity is fixed, it does not hold for elongation at fracture and toughness. It should be noted that lack of fusion pores are far more damaging to these properties because, as Liu et al. explained [23], their irregular shapes result in high localized stress concentrations that cause crack initiation during a tensile test, ultimately leading to premature fracture during plastic strain.

One of the limitations of OM microscopy is that it is fundamentally a 2D technique. This means that for highly porous samples, lack of fusion pores that appear as individual pores on an OM image might actually be interconnected with one another and form a large single 3D network-like pore, as opposed to denser samples where lack of fusion pores (if present) that appear on OM images tend to be truly isolated from one another. Sample 30I, which is the worst performing sample in the mechanical tests due to its high porosity (with ~ 14%), is an example of the former. Figure 12 shows the fracture surfaces of Sample 30I (CF: 0.49, P: 14.1%) after Charpy and tensile testing. Figure 12a (which is the same OM image from Fig. 4f included here for ease of comparison) shows the extent of the lack of fusion porosity as captured in 2D using OM. After fracture from the Charpy and tensile tests, as can be observed in Fig. 12c, d, the fracture surfaces are filled with interconnected pores in 3D that appear to form channels across the material. A higher magnification image of the pores in Fig. 12b after fracture reveals the presence of countless unmelted powder, which is characteristic of lack of fusion due to inadequate melting. In comparison, 60H (CF: 0.60, P: 1.19%), as was shown in Figs. 4j and 9b, d, contains mostly isolated lack of fusion pores. In this case, the fracture surface (Fig. 10b) shows fracture paths that have propagated from one pore to another as opposed to the channels of pre-existing interconnected lack of fusion pores shown on the fracture surfaces of 30I (Fig. 12c, d) — the latter was identified through the presence of unmelted powder across the entire fracture surface.

Nonetheless, the nature of the lack of fusion pores (whether discrete or interconnected) appears to make little difference to mechanical properties as can be observed by the near-linear relationship between the various mechanical properties and porosity levels in Fig. 9 for samples with lack of fusion pores when the porosity level exceeds 1%. This means that despite the limitation of OM techniques to characterize pores in 3D, the use of OM images to determine the amount (via greyscale thresholding) and the type (via circularity factor analysis) of pores present appears to be useful in predicting the tensile and toughness properties of LPBF Ti-6Al-4V parts, as was illustrated in the figure. This approach to predict mechanical properties, however, would still require several LPBF Ti-6Al-4V samples to be printed using a variety of parameters that can produce near 0% porosity in order to determine a benchmark level for mechanical properties at 0% porosity since variations in microstructure caused by different LPBF processing parameters may affect mechanical properties.

Another interesting observation is the fact that when the porosity levels for each sample were calculated and plotted in relation to their corresponding energy densities, which is a metric commonly used to determine the optimal processing window of LPBF parameters [47], it was found that the 30 µm and 60 µm process parameters do not follow the same trend. This is illustrated in Fig. 13 where the energy density of each sample was calculated using Eq. (1). Namely, at 30 µm layer thickness, the required energy density for low porosity appears to be between 40 and 100 J/mm^3, but at 60 µm layer thickness, the window appears to be between 20 and 50 J/mm^3. Since doubling the layer thickness simply halves the energy density, and since the optimal process window is also shifted by a factor of half, it appears that if a parameter set results in very low porosity at 30 µm layer thickness, doubling the layer thickness to 60 µm without altering any other process parameters may still result in a sample with very low porosity.

The relationship between porosity and energy density from the 30- and 60 µm samples highlights a limitation of the energy density equation in that it assumes that energy from the laser is uniformly distributed across a cubic volume but the actual melt pool shape is near-conical and will protrude deeper than a single powder layer [48]. The comparison between 30F (CF: 0.85, P: 0.05%), which is the optimized parameter set, and 60F (CF 0.69. P: 0.06%) best highlights this limitation since both samples were built with the same process parameters except that the latter has double the layer thickness at 60 µm. Both samples have essentially the same amount of porosity despite 60F being built with half the energy density of 30F (28 J/mm^3 vs 56 J/mm^3). Their respective mechanical properties are summarized in Table 5, and their tensile behaviors can be observed in Fig. 6. Overall, both displayed similar mechanical properties except that 60F has a marginally higher yield strength (~ 2.8% more) but lower toughness (~ 16.5% less) and elongation at fracture (~ 17.9% less).

In order to determine if microstructure was the main reason for the observed difference between 30 and 60F, since this could technically explain the strength/ductility trade-off observed here, BSE imaging was conducted. These samples were taken from the undeformed regions of the failed Charpy samples and the images are shown in Fig. 14a, b. As can be observed, the microstructure between the samples appear to be very similar and therefore, is unlikely to be a major contributor to the difference observed. The fracture surfaces, shown in Fig. 14c, d, also appear very similar which indicates that microstructural features are unlikely to be the reason for differences in the mechanical properties. In both cases, the fracture surfaces also reveal some pores. It is worth recalling that as mentioned prior, Sample 60F contains a CF of 0.69 and is thus classified with other samples as having predominately lack of fusion pores for the purposes of predicting mechanical properties. One example of such a pore is shown by the OM image in Fig. 14e. These pores tend to be quite small, and thus, it is uncertain if they are caused by lack of fusion. Regardless, the lower average pore sphericity in 60F could explain its lower ductility results.
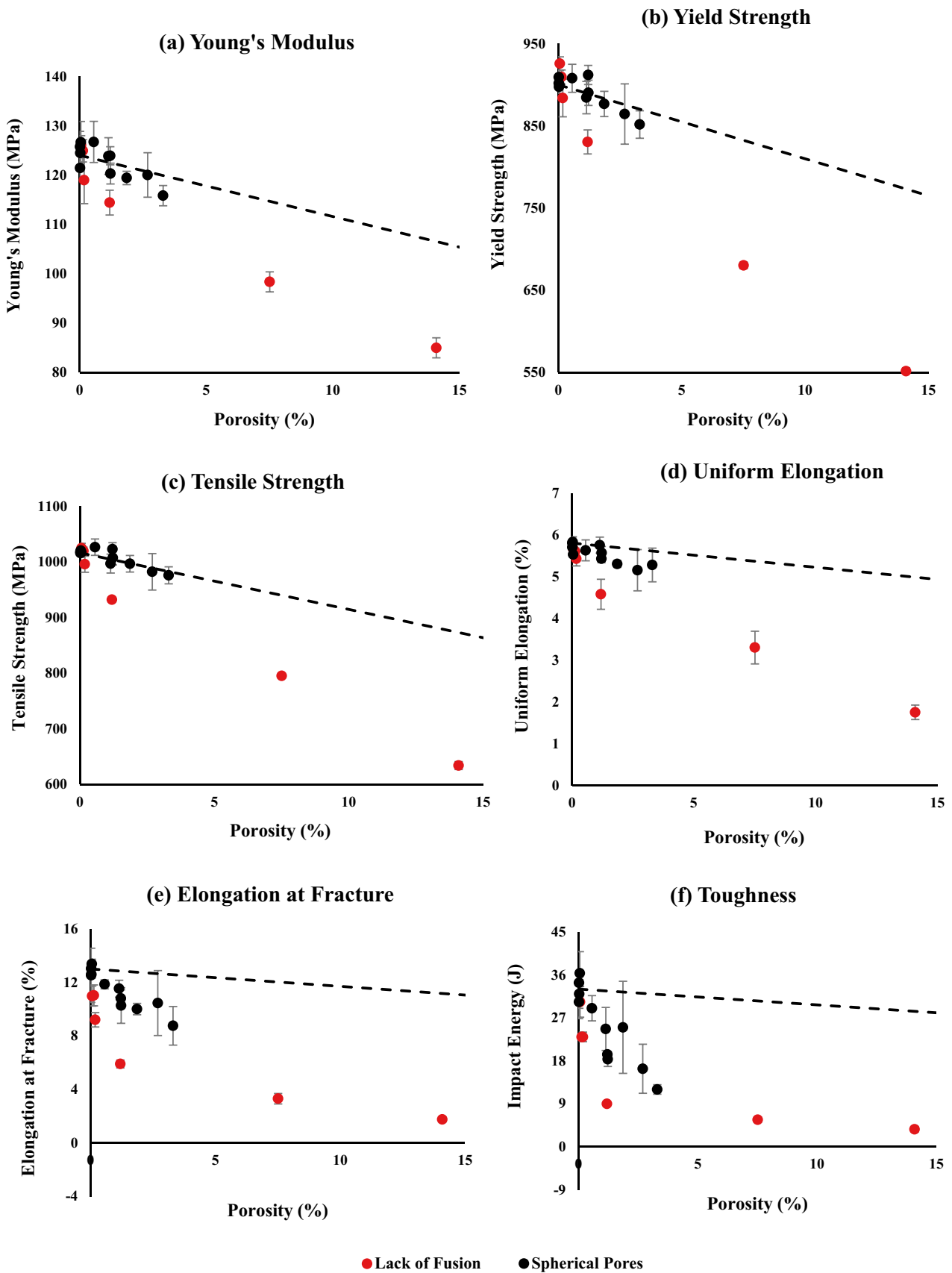
(a) Young's Modulus

(b) Yield Strength

(c) Tensile Strength

(d) Uniform Elongation

(e) Elongation at Fracture

(f) Toughness

● Lack of Fusion　　● Spherical Pores

As mentioned earlier, lack of fusion pores are often identified based on their irregular morphology and large size as there is a large overlap between lack of fusion pores and gas/keyhole pores at intermediate sphericities/circularities (i.e., the ambiguous region) [31]. Therefore, while a sample with an average pore CF of less than 0.70 is unlikely to actually contain lack of fusion pores if it has a very low porosity level, it appears that this threshold is still very useful for predicting mechanical properties since Sample 60F does have a much lower elongation at fracture compared to other samples of similar porosity level but with predominately spherical pores, and its toughness is essentially at the lowest end among those samples. However, the excellent yield strength, tensile strength, and uniform elongation of 60F can be entirely attributed to its microstructure due to its low porosity level. Therefore, even at very low porosity levels where lack of fusion pores do not occur, reduced sphericity of gas/keyhole pores can still have a detrimental effect on ductility and toughness. Regarding 30F and 60F specifically, the doubling of the layer thickness may not have increased the amount of pores significantly, but it did change the morphology of the pores that resulted in worse ductility and toughness (the difference in strength is marginal). Thus, process optimization studies aimed at deriving the process parameters that can achieve near-fully dense parts should also consider the morphology of the very few pores that do form.

Despite the importance of layer thickness in the LPBF process, Fotovvati, Balasubramanian and Asadi commented that many process optimization studies often exclude layer thickness as part of the investigation [18]. To further complicate matters, LPBF parameters that result in the same energy density can result in different melt-pool dimensions [49] though the energy density approach is generally more reliable for determining melt-pool width but not melt-pool depth [50]. Additionally, the layer thickness in LPBF is the distance by which the build plate moves after a single layer is scanned, but the depth of powder deposited every layer is often much larger. Wischeropp et al. showed that for stainless steel, the true powder depth is approximately 225 μm and approximately 165 μm when using a layer thickness of 50 μm and 30 μm, respectively [51]. Therefore, doubling the layer thickness from 30 to 60 μm does not mean that the depth (or volume) of powder that will be melted each layer is doubled. When this is taken into account, a more reliable method of determining the processing window can be developed. For instance, Liu, Fang, and Lei incorporated the true powder depth concept into their analytical model

and were able to predict the processing window required to obtain near-fully dense LPBF Ti-6Al-4V parts that works consistently regardless of the layer thickness used [52].

While this study has focused mainly on the role that porosities can play on the mechanical properties of LPBF Ti-6Al-4V parts, variations in microstructure caused by differences in processing parameters cannot be fully discounted especially at low porosity levels. This is because a typical strength/ductility trade-off was observed with some samples that contain near 0% porosity. Since variations in the processing parameters affect thermal history and cooling rate, the initial β grain formation and the subsequent α' transformation upon cooling can be expected to be slightly different between the samples [53, 54]. This would then have an influence on the final α/β microstructure after α' decomposition during heat-treatment. Nonetheless, the purpose of this study is to evaluate the influence that porosity plays on tensile and toughness properties, and thus, investigations into microstructural variations are outside the scope of this study since the type and amount of pores were the main determinant of mechanical properties in most of the samples investigated.

The results of this study also indicate that it is possible to fabricate samples with very low porosity at 60 μm layer thickness without changing the typical parameters that have been optimized for a layer thickness of 30 μm on the EOS M290. This can essentially half the build time of the LPBF process without a corresponding detriment to mechanical properties (though a slight strength/ductility trade-off might occur). Other methods of improving build speed (i.e., increasing scan speed or decreasing hatch spacing) are not only less efficient, but also generally result in porosity formation and consequently poorer mechanical properties. This is evident in the fact that the typical energy density equation used for determining the processing window for highly dense parts works very well when scan speed and hatch spacing are the parameters being changed, but not when layer thickness is the parameter changed. In fact, the processing window derived using this approach only works for a given layer thickness. Nonetheless, larger layer thicknesses also result in trade-offs with geometric accuracies and roughness. This can be mitigated, as was shown in this study, through the use of an adaptive LPBF process where areas of concern are built with a standard 30 μm parameter set and the bulk of the component can be built using a 60 μm parameter set to reduce build time.

If the load distribution within the bulk of the component during service is known, then based on the results of this study, it may be acceptable for certain regions in a component to contain some amount of porosity, as long as the pores are spherical (i.e., not lack of fusion). This is because the influence of spherical pores to yield strength, tensile strength, and uniform elongation appear to be marginal and can be linearly related to the amount of porosity present. On the other hand, where toughness (and perhaps total
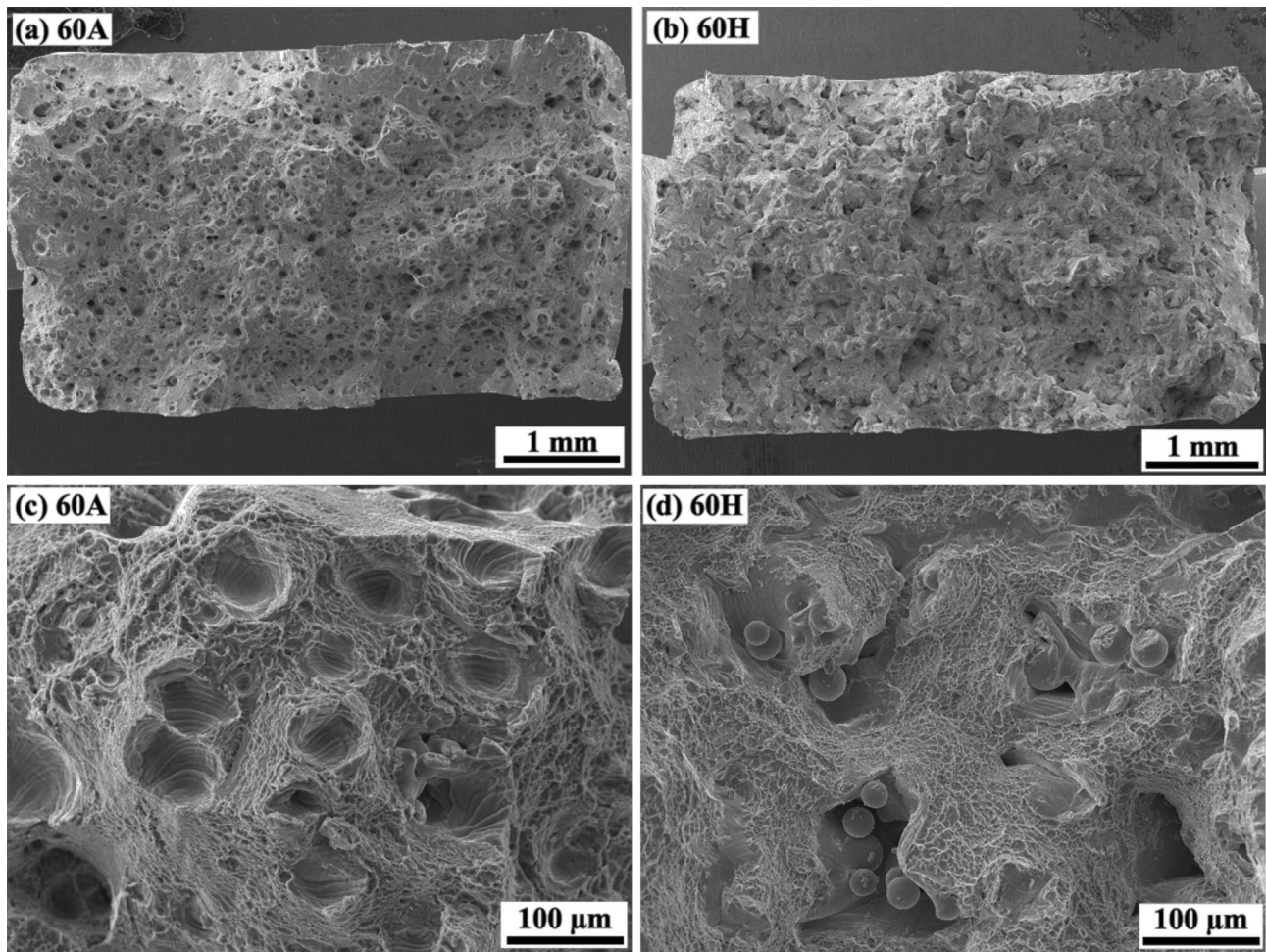
Fig. 10 SEM images showing the fracture surfaces of 60A (CF: 0.80, P: 3.3%) and 60H (CF: 0.60, P: 1.19%) after tensile testing where (**a**) and (**b**) are low magnification SEM images of Samples 60A and H, respec-

tively, while (**c**) and (**d**) show their corresponding high magnification SEM images. 60A and 60H contain~1.2% porosity but the former pores are mostly spherical and the latter pores are mostly irregular in shape

elongation) is a concern, porosity should be minimized as far as possible. Nonetheless, since lack of fusion pores can occur when pursuing much faster LPBF build speeds, such parameters may be utilized at regions of a component with extremely minimal mechanical requirements especially due to the unpredictability of the mechanical results in this case. Thus, depending on the necessity of the localized mechanical requirements at various regions of a component, different sets of parameters can be used across the component (i.e., adaptive LPBF) to maximize build speed while allowing the component to function effectively in service. While this was shown to be viable on a small scale (for instance, in Fig. 2),

the present work is a proof of concept for the viability of the use of two separate parameters in different regions of the same component and to also understand the effects on bulk mechanical performance for regions where a faster process parameter set is used (especially if porosity is formed in the process). Thus, while there is no discernible difference observed near the boundary where the two different process parameter sets intersect, further studies are necessary to confirm if this remains true when scaled up this for complex-shaped components. Furthermore, the influence of using different processing parameter sets on residual stresses and dimensional distortion will also need to be considered.

Table 4 Comparison of the mechanical properties of 30B and 60C

	Young's modulus (MPa)	Yield strength (MPa)	Tensile strength (MPa)	Uniform elongation (%)	Elongation at fracture (%)	Toughness (J)
30B (CF: 0.76, P: 1.14%)	124 ± 4	885 ± 20	997 ± 17	5.8 ± 0.2	11.5 ± 0.6	24.7 ± 4.5
60C (CF: 0.76, P: 1.22%)	120 ± 2	890 ± 15	1007 ± 13	5.6 ± 0.2	10.3 ± 1.3	18.3 ± 1.5

Fig. 11 SEM images showing the fracture surfaces after Charpy impact testing of **a** 30B and **b** 60C
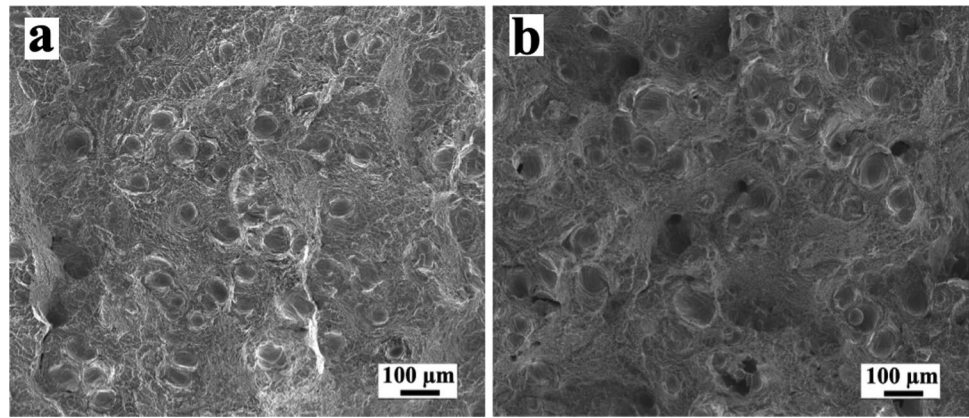

It should also be noted that while the LPBF system used in this study, the EOS M290, is only equipped with a single 400-W laser source, the adaptive LPBF approach recommended in this study is also relevant for high power (~1000 W), multi-laser LPBF systems. Such systems may allow for larger layer thicknesses and faster scan speeds to be explored to further reduce build times, assuming that the challenges of using high laser power can be mitigated. Additionally, the results of this study can also be very useful for quality control of built parts using the relatively inexpensive and simple optical microscopy approach as compared other methods such as X-ray computed tomography [55]. Assuming that a simple optical microscope analysis reveals an unexpected amount pores in a component, the degree of detriment to mechanical properties may be estimated if the pores are generally spherical while the presence of lack of fusion pores could warrant rejection.

For 60 μm parameter sets, the use of layer skipping would also mean an additional time delay between layers due to the additional re-coating time. Based on the build time estimates presented in Fig. 3b, each additional re-coat adds ~10 s to a given build. One possible concern regarding the effect of this additional delay is whether it can influence the cooling rate. However, it is important to note that the time delay between layers is also dependent on the scan area at each layer for a given processing parameter set used. This means that for an

Fig. 12 Fractography images of 30I where **a** is the same OM image from Fig. 4f obtained from the metallographic sample which is included here for reference, **b** is a high magnification SEM image showing a lack of fusion pore revealed after Charpy testing, **c** low magnification SEM image after Charpy impact testing, and **d** low magnification SEM image after tensile testing
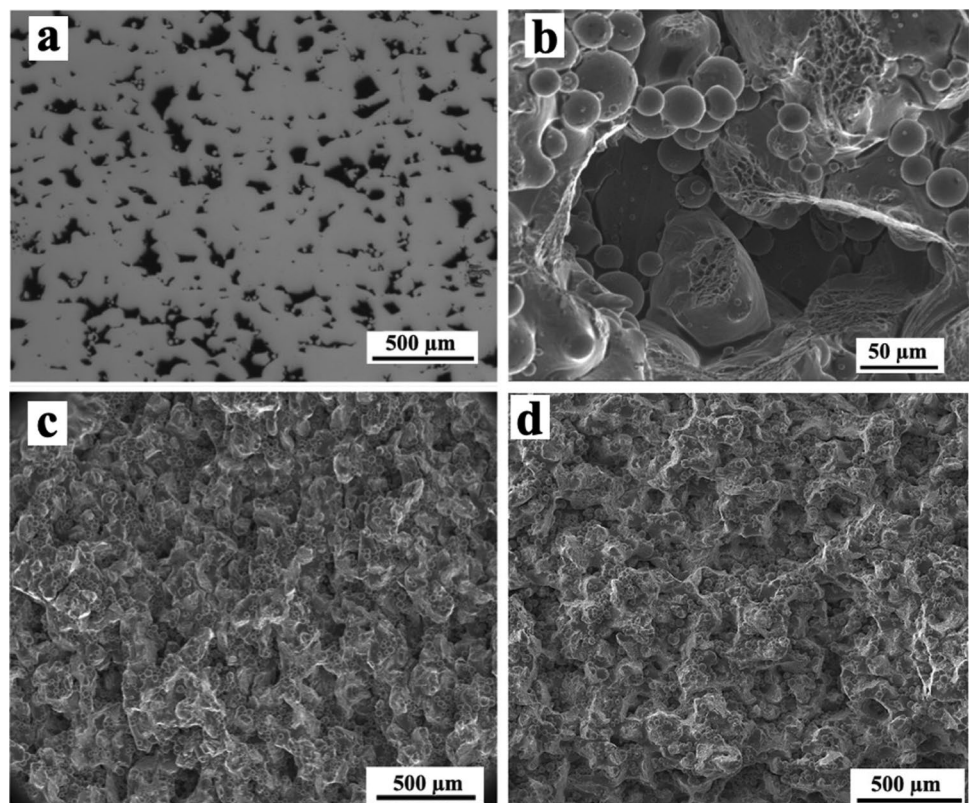
actual complex-shaped component, the time delay between scans will inherently not be the same at each layer. Nonetheless, based on our build time estimate assumption (10% build volume with a uniform scan area across a 150-mm height), the fastest 60 μm parameter set (60 H) takes ~47 s to scan each layer, and layer skipping adds ~10 s to that time. Considering the extremely fast cooling rate of the LPBF process, which is expected to be at least in the order of 10^5 °C/s [56, 57], it is extremely unlikely that layer skipping would result in a considerable difference in the cooling rate, even if the scan area for a given layer is smaller than the assumed 10%. Additionally, given the small amount of thermal energy in the melt pool relative to the large part, most of the cooling occurs immediately after the laser passes over. For a given processing parameter set, the main factors that affect the cooling rate (note that this is still within the order of 10^5 °C/s), and therefore, the resulting microstructure and residual stresses will be the component geometry and the powder bed heating temperature [56].

Lastly, the process inefficiency of the lattice structure approach can also be highlighted here. Based on the study by

Fig. 14 BSE images showing the lamellar microstructure consisting ▶ of α (dark) and β (bright) grains of samples **a** 30F and **b** 60F, and secondary electron images showing the tensile fracture surfaces of **c** 30F and **d** 60F, and an optical microscope image showing an irregular-shaped pore in 60F with a length of ~40 μm

Flores et al. [22], to halve the build time of the bulk region, if a lattice structure was used, it would have to have a volume fraction reduction of 70%. In fact, it should be noted that their study was based on an even smaller layer thickness of 25 μm for the required feature size of the lattice structure, whereas even the optimal parameter set (30F) used in this study utilized a slightly larger layer thickness at 30 μm. This is in contrast with the 60F parameter set where essentially the same amount of time saving was achieved by doubling the layer thickness to 60 μm but without any compromise to volume fraction, and by extension, resulted in only a slight decrease in ductility and toughness. This further highlight that lattice structures are mainly useful only when weight-reduction is the objective but not when process efficiency with minimal compromise to mechanical properties is desired.

Fig. 13 Relationship between energy density and the resulting porosity level of the samples investigated in this study. The optimized parameter set shown here is 30F
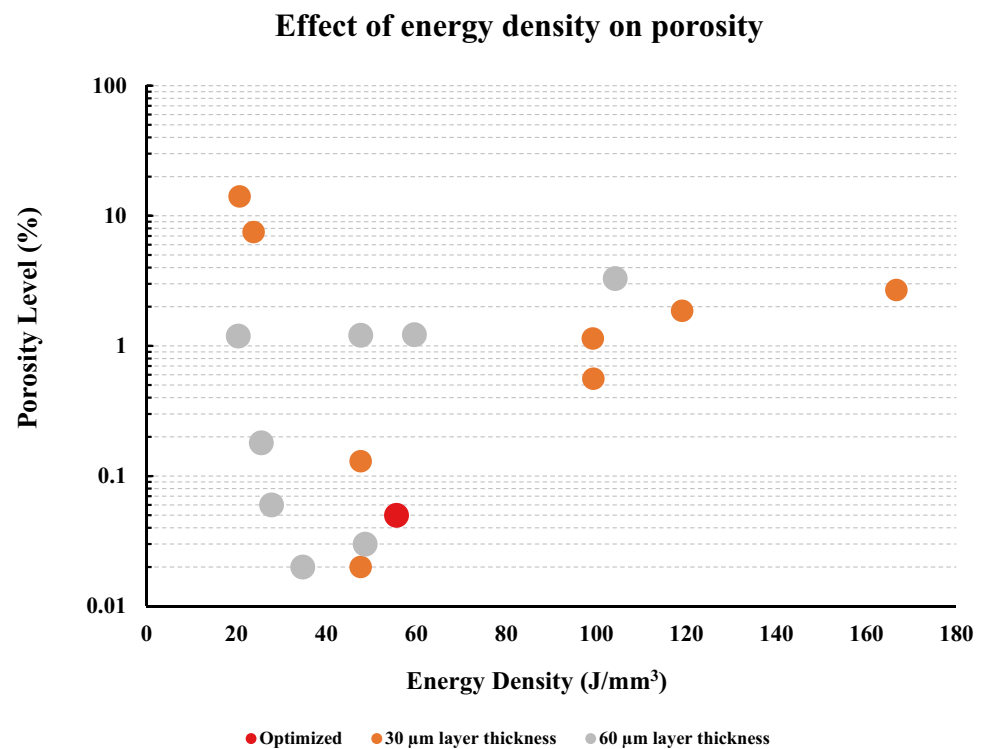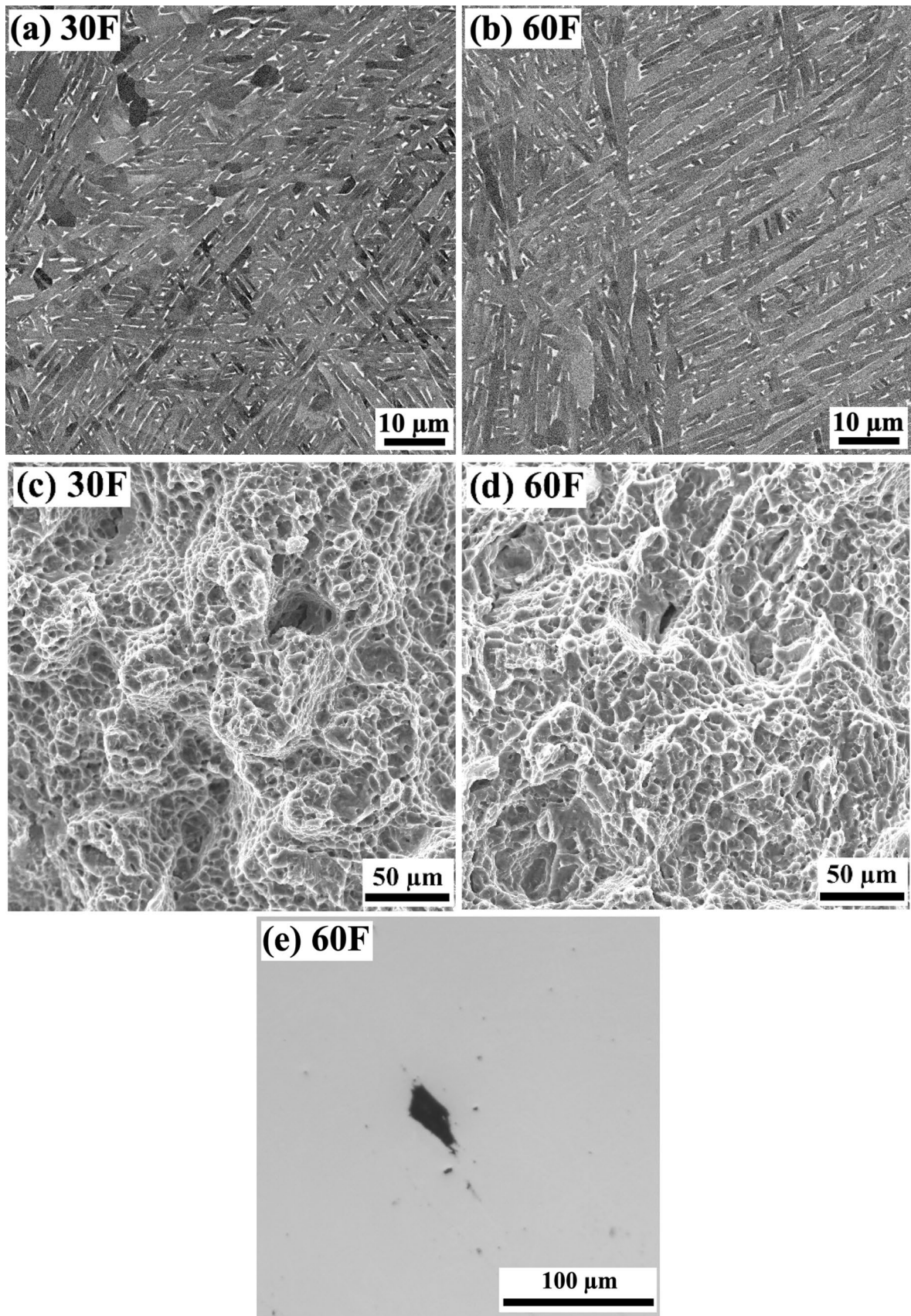

Effect of energy density on porosity

Table 5 Comparison of the mechanical properties of 30F and 60F

	Young's modulus (MPa)	Yield strength (MPa)	Tensile strength (MPa)	Uniform elongation (%)	Elongation at fracture (%)	Toughness (J)
30F (CF: 0.85, P: 0.05%)	127±4	900±3	1017±3	5.5±0.1	13.4±0.4	36.3±4.5
60F (CF: 0.69, P: 0.06%)	126±2	926±8	1025±9	5.7±0.1	11.0±0.7	30.3±3.2

4 Conclusion

This study investigates the effect that porosity plays on tensile and toughness properties of Ti-6Al-4V parts fabricated using laser powder bed fusion (LPBF) with the aim of developing a better understanding on the potential trade-offs when pursuing process efficiency (i.e., faster build times). All samples investigated were heat-treated at 800 °C for 6 h to reflect the typical microstructure that LPBF Ti-6Al-4V components would utilize in service. The Charpy and tensile test samples were built horizontally aligned along the X-axis of the platform. The results of this study can be summarized as follows:

- At near 0% porosity, there was some variation in Young's modulus, yield strength, elongation at fracture, and toughness results. These variations can be attributed solely to microstructure variations. On the other hand, tensile strength and uniform elongation were much more similar across these samples.
- Using optical microscopy to analyze pores across the vertical plane (*YZ* plane) of the samples (i.e., the crack propagation plane in the tensile and Charpy tests), it was found that the average porosity circularity factor was an effective method to quickly distinguish samples that contain predominately irregular (usually, lack of fusion) pores as opposed to samples that contain predominately spherical ones (typically gas or keyhole pores) for the purposes of predicting mechanical properties. If the average circularity factor of pores in a given sample is 0.7 or more, it would be identified as the latter.
- Based on the irregular vs spherical pore distinction, two very specific trends could be observed with all the mechanical properties investigated. Generally speaking, for similar porosity levels, samples that predominately contain irregular pores would perform worse than samples that contain predominately spherical pores. The size of the pores itself had little influence, nor does the nature of the irregular pores (i.e., discrete vs interconnected).
- For samples that contain spherical pores, the linear rule of mixtures relationship held true for Young's modulus, yield strength, and tensile strength. To a certain extent, uniform elongation was also closely related to the linear rule of mixtures. While elongation at fracture and toughness also displayed near-linear relationships with porosity level, the decrease in these properties was far more substantial than would be expected based on the rule of mixtures.
- This study also showed the possibility of an adaptive LPBF approach where different regions of a single component can be built using different processing parameters based on the loading requirements at each region. Where surface roughness is a concern, a 30 µm layer thickness can be used, while most other regions can be built using 60 µm layer thickness parameters to reduce build time. For regions with minimal stress loadings in service where some amount of pores is acceptable, even faster parameters can also be used as long as lack of fusion pores are not formed. However, it should be noted that regions subjected to impact loadings should be built with near-fully dense parameters.

Availability of data and material Available on request.

Declarations

Ethics approval Not applicable.

Consent to participate Not applicable.

Consent for publication All authors consent to the publication of this manuscript.

Conflict of interest Not applicable.

References

1. Barriobero-Vila P, Artzt K, Stark A, Schell N, Siggel M, Gussone J, Kleinert J, Kitsche W, Requena G, Haubrich J (2020) Mapping the geometry of Ti-6Al-4V: from martensite decomposition to localized spheroidization during selective laser melting. Scripta Mater 182:48–52. https://doi.org/10.1016/j.scriptamat.2020.02.043
2. Dutta B, Froes F (2016) Additive manufacturing of titanium alloys: state of the art, challenges and opportunities
3. ASTM (2015) ASTM ISO/ASTM52900-15 standard terminology for additive manufacturing—general principles—terminology
4. Mower TM, Long MJ (2016) Mechanical behavior of additive manufactured, powder-bed laser-fused materials. Mater Sci Eng, A 651:198–213. https://doi.org/10.1016/j.msea.2015.10.068
5. Agius D, Kourousis KI, Wallbrink C (2018) A review of the as-built SLM Ti-6Al-4V mechanical properties towards achieving fatigue resistant designs. Metals 8(1):75. https://doi.org/10.3390/met8010075

6. Shipley H, McDonnell D, Culleton M, Coull R, Lupoi R, O'Donnell G, Trimble D (2018) Optimisation of process parameters to address fundamental challenges during selective laser melting of Ti-6Al-4V: a review. Int J Mach Tools Manuf 128:1–20. https://doi.org/10.1016/j.ijmachtools.2018.01.003

7. Cao S, Chu R, Zhou X, Yang K, Jia Q, Lim CVS, Huang A, Wu X (2018) Role of martensite decomposition in tensile properties of selective laser melted Ti-6Al-4V. J Alloy Compd 744:357–363. https://doi.org/10.1016/j.jallcom.2018.02.111

8. Le V-D, Pessard E, Morel F, Prigent S (2020) Fatigue behaviour of additively manufactured Ti-6Al-4V alloy: the role of defects on scatter and statistical size effect. Int J Fatigue 140:105811. https://doi.org/10.1016/j.ijfatigue.2020.105811

9. Kim WR, Bang GB, Kwon O, Jung K-H, Park H-K, Kim G-H, Jeong H-T, Kim HG (2020) Fabrication of porous pure titanium via selective laser melting under low-energy-density process conditions. Mater Des 195:109035. https://doi.org/10.1016/j.matdes.2020.109035

10. Kan WH, Nadot Y, Foley M, Ridosz L, Proust G, Cairney JM (2019) Factors that affect the properties of additively-manufactured AlSi10Mg: porosity versus microstructure. Addit Manuf 29:100805. https://doi.org/10.1016/j.addma.2019.100805

11. Matilainen V, Piili H, Salminen A, Syvänen T, Nyrhilä O (2014) Characterization of process efficiency improvement in laser additive manufacturing. Phys Procedia 56:317–326. https://doi.org/10.1016/j.phpro.2014.08.177

12. Dilip J, Zhang S, Teng C, Zeng K, Robinson C, Pal D, Stucker B (2017) Influence of processing parameters on the evolution of melt pool, porosity, and microstructures in Ti-6Al-4V alloy parts fabricated by selective laser melting. Prog Addit Manuf 2(3):157–167. https://doi.org/10.1007/s40964-017-0030-2

13. Zafari A, Barati MR, Xia K (2019) Controlling martensitic decomposition during selective laser melting to achieve best ductility in high strength Ti-6Al-4V. Mater Sci Eng, A 744:445–455. https://doi.org/10.1016/j.msea.2018.12.047

14. Montero-Sistiaga ML, Godino-Martinez M, Boschmans K, Kruth J-P, Van Humbeeck J, Vanmeensel K (2018) Microstructure evolution of 316L produced by HP-SLM (high power selective laser melting). Addit Manuf 23:402–410. https://doi.org/10.1016/j.addma.2018.08.028

15. Pal S, Lojen G, Hudak R, Rajtukova V, Brajlih T, Kokol V, Drstvenšek I (2020) As-fabricated surface morphologies of Ti-6Al-4V samples fabricated by different laser processing parameters in selective laser melting. Addit Manuf 33:101147. https://doi.org/10.1016/j.addma.2020.101147

16. Chen Z, Wu X, Tomus D, Davies CHJ (2018) Surface roughness of selective laser melted Ti-6Al-4V alloy components. Addit Manuf 21:91–103. https://doi.org/10.1016/j.addma.2018.02.009

17. Attarzadeh F, Fotovvati B, Fitzmire M, Asadi E (2020) Surface roughness and densification correlation for direct metal laser sintering. The International Journal of Advanced Manufacturing Technology 107(5):2833–2842. https://doi.org/10.1007/s00170-020-05194-0

18. Fotovvati B, Balasubramanian M, Asadi E (2020) Modeling and optimization approaches of laser-based powder-bed fusion process for Ti-6Al-4V alloy. Coatings 10(11). https://doi.org/10.3390/coatings10111104

19. Wycisk E, Siddique S, Herzog D, Walther F, Emmelmann C (2015) Fatigue performance of laser additive manufactured Ti–Al–4V in very high cycle fatigue regime up to 109 cycles. Front Mater 2:72. https://doi.org/10.3389/fmats.2015.00072

20. Benedetti M, Torresani E, Leoni M, Fontanari V, Bandini M, Pederzolli C, Potrich C (2017) The effect of post-sintering treatments on the fatigue and biological behavior of Ti-6Al-4V ELI parts made by selective laser melting. J Mech Behav Biomed Mater 71:295–306. https://doi.org/10.1016/j.jmbbm.2017.03.024

21. Andreau O, Pessard E, Koutiri I, Penot J-D, Dupuy C, Saintier N, Peyre P (2019) A competition between the contour and hatching zones on the high cycle fatigue behaviour of a 316L stainless steel: analyzed using X-ray computed tomography. Mater Sci Eng A 757:146–159. https://doi.org/10.1016/j.msea.2019.04.101

22. Flores I, Kretzschmar N, Azman AH, Chekurov S, Pedersen DB, Chaudhuri A (2020) Implications of lattice structures on economics and productivity of metal powder bed fusion. Addit Manuf. https://doi.org/10.1016/j.addma.2019.100947

23. Liu W, Chen C, Shuai S, Zhao R, Liu L, Wang X, Hu T, Xuan W, Li C, Yu J, Wang J, Ren Z (2020) Study of pore defect and mechanical properties in selective laser melted Ti6Al4V alloy based on X-ray computed tomography. Mater Sci Eng A 797:139981. https://doi.org/10.1016/j.msea.2020.139981

24. Kaschel FR, Celikin M, Dowling DP (2020) Effects of laser power on geometry, microstructure and mechanical properties of printed Ti-6Al-4V parts. J Mater Process Technol 278:116539. https://doi.org/10.1016/j.jmatprotec.2019.116539

25. Montalbano T, Briggs BN, Waterman JL, Nimer S, Peitsch C, Sopcisak J, Trigg D, Storck S (2021) Uncovering the coupled impact of defect morphology and microstructure on the tensile behavior of Ti-6Al-4V fabricated via laser powder bed fusion. J Mater Process Technol 294:117113. https://doi.org/10.1016/j.jmatprotec.2021.117113

26. Zhao X, Li S, Zhang M, Liu Y, Sercombe TB, Wang S, Hao Y, Yang R, Murr LE (2016) Comparison of the microstructures and mechanical properties of Ti–6Al–4V fabricated by selective laser melting and electron beam melting. Mater Des 95:21–31. https://doi.org/10.1016/j.matdes.2015.12.135

27. Pal S, Gubeljak N, Hudak R, Lojen G, Rajtukova V, Predan J, Kokol V, Drstvensek I (2019) Tensile properties of selective laser melting products affected by building orientation and energy density. Mater Sci Eng A 743:637–647. https://doi.org/10.1016/j.msea.2018.11.130

28. Wu M-W, Lai P-H, Chen J-K (2016) Anisotropy in the impact toughness of selective laser melted Ti–6Al–4V alloy. Mater Sci Eng A 650:295–299. https://doi.org/10.1016/j.msea.2015.10.045

29. Vilardell AM, Fredriksson G, Yadroitsev I, Krakhmalev P (2019) Fracture mechanisms in the as-built and stress-relieved laser powder bed fusion Ti6Al4V ELI alloy. Opt Laser Technol 109:608–615. https://doi.org/10.1016/j.optlastec.2018.08.042

30. Wu M-W, Lai P-H (2016) The positive effect of hot isostatic pressing on improving the anisotropies of bending and impact properties in selective laser melted Ti-6Al-4V alloy. Mater Sci Eng A 658:429–438. https://doi.org/10.1016/j.msea.2016.02.023

31. Snell R, Tammas-Williams S, Chechik L, Lyle A, Hernández-Nava E, Boig C, Panoutsos G, Todd I (2020) Methods for rapid pore classification in metal additive manufacturing. JOM 72(1):101–109. https://doi.org/10.1007/s11837-019-03761-9

32. ASTM (2016) ASTM E8 / 8M - 16a Standard Test Methods for Tension Testing of Metallic Materials

33. Zhang S, Rauniyar S, Shrestha S, Ward A, Chou K (2019) An experimental study of tensile property variability in selective laser melting. J Manuf Process 43:26–35. https://doi.org/10.1016/j.jmapro.2019.03.045

34. Sanaei N, Fatemi A, Phan N (2019) Defect characteristics and analysis of their variability in metal L-PBF additive manufacturing. Mater Des 182:108091. https://doi.org/10.1016/j.matdes.2019.108091

35. Ji S, Gu Q, Xia B (2006) Porosity dependence of mechanical properties of solid materials. J Mater Sci 41(6):1757–1768. https://doi.org/10.1007/s10853-006-2871-9

36. Yadollahi A, Shamsaei N (2017) Additive manufacturing of fatigue resistant materials: Challenges and opportunities. Int J Fatigue 98:14–31. https://doi.org/10.1016/j.ijfatigue.2017.01.001

37. Günther J, Leuders S, Koppa P, Tröster T, Henkel S, Biermann H, Niendorf T (2018) On the effect of internal channels and surface roughness on the high-cycle fatigue performance of Ti-6Al-4V processed by SLM. Mater Des 143:1–11. https://doi.org/10.1016/j.matdes.2018.01.042

38. Nadot Y, Nadot-Martin C, Kan WH, Boufadene S, Foley M, Cairney J, Proust G, Ridosz L (2020) Predicting the fatigue life of an AlSi10Mg alloy manufactured via laser powder bed fusion by using data from computed tomography. Addit Manuf 32:100899. https://doi.org/10.1016/j.addma.2019.100899

39. Shore RJ, McCauley RB (1970) Effects of porosity on high strength aluminum 7039. Paper presented at the 51th Annual Meeting Cleveland, Ohio

40. Voisin T, Calta NP, Khairallah SA, Forien J-B, Balogh L, Cunningham RW, Rollett AD, Wang YM (2018) Defects-dictated tensile properties of selective laser melted Ti-6Al-4V. Mater Des 158:113–126. https://doi.org/10.1016/j.matdes.2018.08.004

41. Hayden HW, Moffatt WG, Wulff J (1965) The structure and properties of materials, vol III. John Wiley & Sons Inc, New York

42. Stef J, Poulon-Quintin A, Redjaimia A, Ghanbaja J, Ferry O, De Sousa M, Gouné M (2018) Mechanism of porosity formation and influence on mechanical properties in selective laser melting of Ti-6Al-4V parts. Mater Des 156:480–493. https://doi.org/10.1016/j.matdes.2018.06.049

43. Moletsane MG, Krakhmalev P, Kazantseva N, Du Plessis A, Yadroitsava I, Yadroitsev I (2016) Tensile properties and microstructure of direct metal laser-sintered Ti6Al4V (ELI) alloy. S Afr J Ind Eng 27(3):110–121

44. Grell WA, Solis-Ramos E, Clark E, Lucon E, Garboczi EJ, Predecki PK, Loftus Z, Kumosa M (2017) Effect of powder oxidation on the impact toughness of electron beam melting Ti-6Al-4V. Addit Manuf 17:123–134. https://doi.org/10.1016/j.addma.2017.08.002

45. Keshavarz MK, Sikan F, Boutet CE, Milligan J, Bois-Brochu A, Brochu M (2019) Impact properties of half stress-relieved and hot isostatic pressed Ti–6Al–4V components fabricated by laser powder bed fusion. Mater Sci Eng A 760:481–488. https://doi.org/10.1016/j.msea.2019.05.035

46. Kunigita M, Aihara S, Kawabata T, Kasuya T, Okazaki Y, Inomoto M (2020) Prediction of Charpy impact toughness of steel weld heat-affected zones by combined micromechanics and stochastic fracture model – Part I: Model presentation. Eng Fract Mech 230:106965. https://doi.org/10.1016/j.engfracmech.2020.106965

47. Xu W, Sun S, Elambasseril J, Liu Q, Brandt M, Qian M (2015) Ti-6Al-4V additively manufactured by selective laser melting with superior mechanical properties. Jom 67(3):668–673. https://doi.org/10.1007/s11837-015-1297-8

48. Pal S, Lojen G, Kokol V, Drstvensek I (2018) Evolution of metallurgical properties of Ti-6Al-4V alloy fabricated in different energy densities in the Selective Laser Melting technique. J Manuf Process 35:538–546. https://doi.org/10.1016/j.jmapro.2018.09.012

49. Mishra AK, Kumar A (2019) Numerical and experimental analysis of the effect of volumetric energy absorption in powder layer on thermal-fluidic transport in selective laser melting of Ti6Al4V. Opt Laser Technol 111:227–239. https://doi.org/10.1016/j.optlastec.2018.09.054

50. Scipioni Bertoli U, Wolfer AJ, Matthews MJ, Delplanque J-PR, Schoenung JM (2017) On the limitations of volumetric energy density as a design parameter for Selective Laser Melting. Mater Des 113:331–340. https://doi.org/10.1016/j.matdes.2016.10.037

51. Wischeropp TM, Emmelmann C, Brandt M, Pateras A (2019) Measurement of actual powder layer height and packing density in a single layer in selective laser melting. Addit Manuf 28:176–183. https://doi.org/10.1016/j.addma.2019.04.019

52. Liu B, Fang G, Lei L (2021) An analytical model for rapid predicting molten pool geometry of selective laser melting (SLM). Appl Math Model 92:505–524. https://doi.org/10.1016/j.apm.2020.11.027

53. Ali H, Ghadbeigi H, Mumtaz K (2018) Processing parameter effects on residual stress and mechanical properties of selective laser melted Ti6Al4V. J Mater Eng Perform 27(8):4059–4068. https://doi.org/10.1007/s11665-018-3477-5

54. Khorasani A, Gibson I, Awan US, Ghaderi A (2019) The effect of SLM process parameters on density, hardness, tensile strength and surface quality of Ti-6Al-4V. Addit Manuf 25:176–186. https://doi.org/10.1016/j.addma.2018.09.002

55. Romano S, Abel A, Gumpinger J, Brandão A, Beretta S (2019) Quality control of AlSi10Mg produced by SLM: metallography versus CT scans for critical defect size assessment. Addit Manuf 28:394–405. https://doi.org/10.1016/j.addma.2019.05.017

56. Ali H, Ghadbeigi H, Mumtaz K (2018) Residual stress development in selective laser-melted Ti6Al4V: a parametric thermal modelling approach. Int J Adv Manuf Technol 97(5):2621–2633. https://doi.org/10.1007/s00170-018-2104-9

57. Yang J, Yu H, Yin J, Gao M, Wang Z, Zeng X (2016) Formation and control of martensite in Ti-6Al-4V alloy produced by selective laser melting. Mater Des 108:308–318. https://doi.org/10.1016/j.matdes.2016.06.117

Publisher's Note Springer Nature remains neutral with regard to jurisdictional claims in published maps and institutional affiliations.